1

Locomotion over a viscoplastic film

SAMUEL S. PEGLER[1] AND NEIL J. BALMFORTH[2]

[1] Institute of Theoretical Geophysics, Department of Applied Mathematics and Theoretical Physics, University of Cambridge, Wilberforce Road, Cambridge CB3 0WA, UK
[2] Department of Mathematics, University of British Columbia, 1984 Mathematics Road, Vancouver, BC, V6T 1Z2, Canada

We present a modelling study of locomotion over a layer of viscoplastic fluid motivated by the self-propulsion of marine and terrestrial gastropods. Our model comprises a layer of viscoplastic mucus lying beneath a fluid-filled foot that is laced internally by muscular fibres under tension and overlain by the main body of the locomotor, which is assumed to be rigid. The mucus is described using lubrication theory and the Bingham constitutive law, and the foot using a continuum approximation for the action of the muscle fibres. The model is first used to study the retrograde strategy of locomotion employed by marine gastropods, wherein the muscle fibres create a backwards-travelling wave of predominantly normal displacements along the surface of the foot. Once such a retrograde forcing pattern is switched on, the system is shown to converge towards a steady state of locomotion in a frame moving with the wave. The steady speed of locomotion decreases with the yield stress, until it vanishes altogether above a critical yield stress. Despite the absence of locomotion above this threshold, waves still propagate along the foot, peristaltically pumping mucus in the direction of the wave. The model is next used to study the prograde strategy employed by terrestrial gastropods, wherein the muscle fibres create a forwards-travelling wave of predominantly tangential displacements of the foot surface. In this case, a finite yield stress is shown to be necessary for locomotion, with the speed of locomotion initially increasing with the yield stress. Beyond a critical yield stress, localized rigid plugs form across the depth of the mucus layer, adhering parts of the foot to the base. These stop any transport of mucus, but foot motions elsewhere still drive locomotion. As the yield stress is increased further, the rigid plugs widen horizontally, increasing the viscous drag and eventually reducing the speed of locomotion, which is therefore maximized for an intermediate value of the yield stress.

1. Introduction

Snails and slugs propel themselves forwards by sending waves of muscular contractions along the base of their foot, which overlays a layer of mucus. This unique form of locomotion allows snails and slugs to traverse almost any obstacle without damage. In particular, the mucus is thought to facilitate their ability to climb steeply inclined surfaces. It has been suggested that the mechanism underlying this ability is associated with the non-Newtonian rheology of the mucus, which is known to have an appreciable yield stress, or minimum stress required to generate fluid-like flow (Denny 1980; Ewoldt *et al.* 2007).

In this paper, we develop a continuum model to explore locomotion over a layer of viscoplastic fluid, investigating two particular locomotion strategies. More specifically,

marine snails often adopt a *retrograde* strategy wherein the foot muscles apply a predominantly normal force in the form of a backwards-travelling wave. The mechanics underlying this strategy are central to many other forms of bio-locomotion and are similar to those that underlie the operation of a peristaltic pump (e.g. Shapiro, Jaffrin &Weinberg 1969). By contrast, terrestrial snails typically adopt a *prograde* strategy whereby the foot muscles apply a predominantly tangential force in the form of a forwards-travelling wave (e.g. Jones 1973; Denny 1981). Our analysis focuses on understanding how the yield stress influences the speed of locomotion in both of these strategies.

Studies of retrograde locomotion strategies in general began with the seminal work of Taylor (1951) who determined the locomotive action of a planar sheet that undulates with normal displacements while immersed in an infinite body of Newtonian fluid. Closer to the geometry of a gastropod is the configuration studied by Katz (1974), who generalized that of Taylor (1951) to allow for a rigid wall lying parallel to the locomotive sheet. This study included a lubrication theory for displacements of the sheet comparable with the distance between the oscillating sheet and the rigid wall. Recently, this theory has been extended by Balmforth, Coombs & Pachman (2010) to allow for a non-Newtonian intervening fluid and to incorporate the elastic dynamics of the deforming sheet.

The only detailed model of prograde locomotion over a fluid film of which we are aware is that proposed by Chan, Balmforth & Hosoi (2005). These authors kinematically impose a wave of tangential displacements of the surface of the foot and study the resulting flow in an underlying layer of viscoplastic fluid. They find that the speed of locomotion is proportional to the mean tangential displacement generated by the wave. However, their model omits any consideration of the detailed balance of forces that act to generate locomotion. In particular, by specifying the foot displacement, their model automatically assumes that locomotion occurs and cannot address its dynamical activation.

In the current article, we build on these earlier studies by formulating a fully dynamic model for the foot and mucus layer of a gastropod. Motivated by studies of gastropod anatomy (e.g. Jones 1973; Denny 1981), our formulation models the foot muscles as strings under tension that can contract to exert both normal and tangential forces at the base of the foot. Following Chan *et al.* (2005) and Balmforth *et al.* (2010), we model the viscoplastic mucus using a Bingham constitutive law and lubrication theory. We subsequently formulate two singular asymptotic limits of our general model, which we use to study separately the dynamics of retrograde and prograde locomotion.

In our analysis of retrograde locomotion, we extend the study of Balmforth *et al.* (2010) by addressing the dynamical activation and behaviour of the locomotor as it evolves from a state of rest. Having determined the conditions for convergence towards steady locomotion, we proceed to explore the dependence of the steady locomotion velocity on the yield stress, the elastic properties of the foot and the amplitude of the muscular forcing. We focus in particular on confirming the hypothesis proposed by Balmforth *et al.* (2010) that a yield stress is generally detrimental to the retrograde locomotion strategy, slowing and even halting locomotion entirely.

Our study of prograde locomotion extends that of Chan *et al.* (2005) by formulating the model in terms of the muscular and elastic forces of the foot. This dynamic formulation shows how the resultant of the forwards forces exerted by the muscle fibres necessarily vanishes, as otherwise there is an unphysical acceleration of the main body of the locomotor relative to the foot. A notable implication is that prograde locomotion is impossible with Newtonian mucus. However, significant locomotion can be activated by combining a yield-stress mucus rheology with muscular forcing patterns that have certain spatial structure.

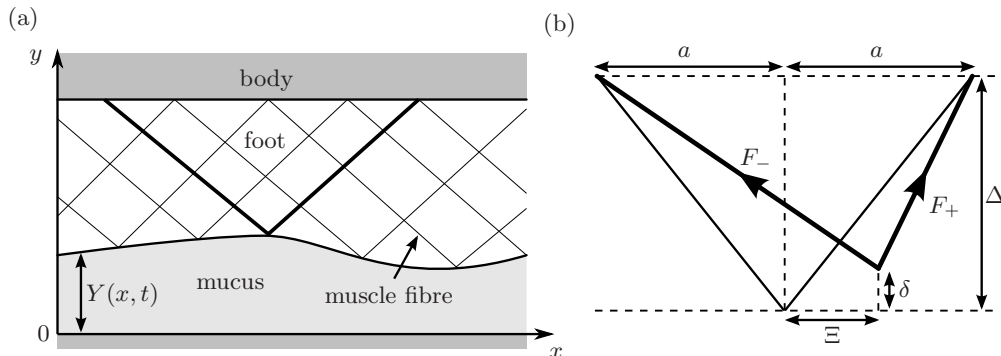We begin in §2 by developing our general thin-film model that describes the elastic

FIGURE 1. Schematic illustration of our model showing (a) the geometry of the foot, mucus and muscle fibres in the foot cavity, and (b) a specific pair of muscle fibres anchored between the body and a point on the foot surface. In (b), the fibre pair is shown in its neutral state (thin) and its perturbed state (thick). The vertical scale has been exaggerated.

mechanics of the foot and the viscoplastic fluid mechanics of the mucus layer. In §3–4, we use a combination of numerical and asymptotic approaches to explore retrograde and prograde strategies. In §5, we compare the two locomotion strategies and discuss why gastropods in marine and terrestrial environments might adopt certain strategies.

2. Theoretical model

The structure of gastropod anatomy has been highlighted from studies of flash-frozen specimens (Jones 1973; Denny 1981). As shown schematically in figure 1, this structure constitutes a flexible foot of characteristic thickness 10^{-3} m that sits atop a layer of mucus of much smaller characteristic thickness 10^{-5} m. These studies indicate that the main body of the gastropod, which lies above the foot, is essentially rigid. We proceed to develop a continuum model of this three-tier system.

2.1. *The foot*

The foot is a pressurized, fluid-filled cavity containing contractible pairs of muscular fibres anchored between the lower surface of the foot and the body in two inclined directions (Jones 1973; Denny 1981). Locomotion is generated by sequential contractions of these muscular fibres, which can exert both normal and tangential resultant forces upon the lower surface of the foot, depending on whether the fibres in each pair are contracted individually or in unison. Images of the underside of a snail undergoing locomotion show that the contractions take the form of travelling waves with characteristic wavelength $2\pi L \approx 0.01$ m and wave speed $c \approx 0.001$ m s^{-1}, respectively (Lai *et al.* 2011). On this basis, we consider only periodic sections of the system of length $2\pi L$, treating each period of the locomotive forcing wave as an identical unit. Neglecting also the edge effects at the sides, front and back of the foot, we consider a two-dimensional cross-section along the length of the system.

Let $y = 0$ and $y = Y(x,t)$ denote the heights of the rigid horizontal surface under the mucus layer and the lower surface of the foot, respectively, and let $\Delta - \delta(x,t)$ denote the thickness of the foot, where Δ is the unperturbed thickness and $\delta \ll \Delta$ is a small vertical displacement. If H is the unperturbed thickness of the mucus layer, then

$$\delta = Y - H. \tag{2.1}$$

Under the assumption that the mucus and the fluid inside the foot cavity are incompressible, conservation of mass demands that

$$\langle Y \rangle = H \quad \text{and} \quad \langle \delta \rangle = 0, \quad \text{where} \quad \langle ... \rangle \equiv \frac{1}{2\pi L} \int_0^{2\pi L} (...) \, dx \qquad (2.2)$$

denotes the mean over one period of the wave. The vertical position of the main body must therefore remain fixed and translate purely horizontally with velocity $U(t)$.

We model the muscular fibres inside the foot as strings under tension, and prescribe contractive forces to these fibres to drive the locomotive waves. Consider a point on the lower surface of the foot at position x. We assume that the ends of the two fibres attached to this point are each separated by an unstretched horizontal distance a, and that the inclinations and horizontal displacements of the fibres are small ($\Delta \ll a$ and $\Xi \ll a$, respectively). The leftward and rightward fibres then have the leading-order extensions

$$[(a \pm \Xi)^2 + (\Delta - \delta)^2]^{1/2} - (a^2 + \Delta^2)^{1/2} \approx \pm\Xi, \qquad (2.3)$$

respectively. If the tensions generated by the fibres are in proportion to their extension (2.3), then the forces in the leftward and rightward fibres are given to leading order by

$$F_\pm = T_0 \mp \Lambda\Xi + T_\pm, \qquad (2.4)$$

where T_0 is the unperturbed tension in each fibre, Λ is an elastic modulus and $T_\pm$ denote the muscular contractive forces that are exerted to drive the locomotive waves. Assuming that the fibres are distributed densely, we treat $F_\pm$ as continuous functions of position and time. The resultant of the forces (2.4) can be resolved into the leading-order horizontal and vertical components,

$$\left[F_+ - F_-, \frac{\Delta - \delta}{a}(F_+ + F_-) \right] \approx \left[-2\Lambda\Xi + T_+ - T_-, \frac{2T_0}{a}(\Delta - \delta) + \frac{\Delta}{a}(T_+ + T_-) \right], \tag{2.5}$$

where we have assumed that $T_+ + T_- = O(\delta T_0/\Delta) \ll T_0$, which is the scale of the applied tension required to generate a vertical foot displacement of order δ.

The fibre force in (2.5) must be balanced by the stresses exerted on the lower surface of the foot by the fluid inside the foot cavity and the mucus. When both of these layers are shallow, the vertical stresses are dominated by the pressures of the foot cavity and mucus, denoted p_C and p respectively. A balance between the vertical forces on the surface of the foot then demands that

$$\frac{2T_0}{a}(\Delta - \delta) + \frac{\Delta}{a}(T_+ + T_-) = p_C - p \qquad \text{(on } y = Y). \qquad (2.6)$$

In view of our assumption that the foot is much thicker than the mucus layer ($\Delta \gg Y$), we treat the cavity pressure p_C as constant compared with the mucus pressure p. For similar reasons, we neglect the viscous traction exerted by the fluid in the foot cavity on the lower surface of the foot. The balance of horizontal forces at the surface of the foot is then given to leading order by

$$2\Lambda\Xi - T_+ + T_- = -\tau - \frac{\partial Y}{\partial x}(p - p_C) \qquad \text{(on } y = Y), \qquad (2.7)$$

where τ is the viscous shear stress exerted by the mucus.

In the absence of any fibre inertia, the net reaction to the force in (2.7) pulls back on the main body of the locomotor, leading to the equation of motion

$$\mathcal{M}\dot{U} = \langle \tau + Y_x(p - p_C) \rangle \qquad \text{(on } y = Y), \qquad (2.8)$$

where $\mathcal{M}$ is the mass of the main body per unit area, and we have used a dot to denote d/dt and an x subscript to denote $\partial/\partial x$, a short-hand notation that we extend to the other partial derivatives below.

2.2. *The mucus layer*

We model the mucus as a thin layer of viscoplastic fluid with negligible inertia (cf. Chan *et al.* 2005; Ewoldt *et al.* 2007; Balmforth *et al.* 2010). On applying the lubrication approximation, the equations of continuity and force balance take the leading-order forms

$$\frac{\partial u}{\partial x} + \frac{\partial v}{\partial y} = 0, \quad \frac{\partial p}{\partial x} = \frac{\partial \tau}{\partial y}, \quad \frac{\partial p}{\partial y} = 0, \qquad (2.9a,b,c)$$

respectively, where u and v are the horizontal and vertical components of the velocity.

We use the Bingham model to describe the yield-stress rheology of the mucus (Bird *et al.* 1983). To leading order, the constitutive relation simplifies to

$$\begin{cases} \tau = \mu \dfrac{\partial u}{\partial y} + \tau_Y \, \mathrm{sgn}\left(\dfrac{\partial u}{\partial y}\right) & |\tau| > \tau_Y, \\[3mm] 0 = \dfrac{\partial u}{\partial y} & |\tau| < \tau_Y, \end{cases} \qquad (2.10a,b)$$

where μ is the dynamic viscosity and τ_Y is the yield stress. Relation $(2.10a)$ applies to fully yielded sections of the fluid, while $(2.10b)$ applies to plug-like sections that have no vertical shear to leading order. Note that $(2.10b)$ need not imply that the fluid forms a truly rigid plug: the full yield condition involves all the components of the stress tensor and, in regions where $(2.10b)$ applies, extensional stresses can become comparable with shear stresses and cause the fluid to yield weakly (Balmforth & Craster 1999). The resulting flow is not a true plug and is more correctly referred to as a *pseudo-plug*. A key difference between the two is that τ is determined in pseudo-plugs, whereas it is formally indeterminate over true plugs, as in classical plasticity theory (Prager & Hodge 1951).

Equation $(2.9c)$ implies that $p = p(x,t)$ only. Integrating $(2.9b)$, we obtain

$$\tau(x,y,t) = \tau_B + y\frac{\partial p}{\partial x} = \tau_S - (Y-y)\frac{\partial p}{\partial x} \qquad (2.11)$$

where $\tau_B \equiv \tau(x,0,t)$ and $\tau_S \equiv \tau(x,Y,t)$ denote the shear stress at the base and foot surface, respectively. The no-slip condition imposed at the surface of the foot determines the vertical and horizontal kinematic surface conditions

$$v(x,Y,t) = \frac{\partial Y}{\partial t} + u_S \frac{\partial Y}{\partial x}, \qquad u(x,Y,t) = u_S = U + \frac{\partial \Xi}{\partial t} + u_S \frac{\partial \Xi}{\partial x}. \qquad (2.12a,b)$$

Combining $(2.12a)$ with the depth integration of $(2.9a)$, we obtain

$$\frac{\partial Y}{\partial t} + \frac{\partial q}{\partial x} = 0, \quad \text{where} \quad q \equiv \int_0^Y u \, \mathrm{d}z \qquad (2.13)$$

is the volumetric flux per unit width of the flow.

2.3. *Dimensionless model system*

We non-dimensionalize the system above by defining

$$(\hat{x}, \hat{\Xi}) \equiv \frac{1}{L}(x, \Xi), \quad (\hat{y}, \hat{Y}) \equiv \frac{1}{H}(y, Y), \quad \hat{t} \equiv \frac{ct}{L}, \quad (\hat{u}, \hat{U}, \hat{u}_S) \equiv \frac{1}{c}(u, U, u_S),$$

$$\hat{q} = \frac{1}{cH}q, \quad \hat{p} \equiv \frac{H^2}{\mu cL}(p - p_C), \quad (\hat{\tau}, \hat{\tau}_S, \hat{\tau}_B) \equiv \frac{H}{\mu c}(\tau, \tau_S, \tau_B). \qquad (2.14)$$

On dropping hats, (2.11) and (2.10) become

$$\tau = \tau_B + yp_x = \tau_S - (Y - y)p_x, \qquad \begin{cases} \tau = u_y + B\operatorname{sgn}(u_y) & |\tau| > B, \\ u_y = 0 & |\tau| < B, \end{cases} \qquad (2.15a,b)$$

where $B \equiv \tau_Y H/\mu c$ is the Bingham number. Equations (2.13) and (2.12b) remain as

$$Y_t + q_x = 0, \qquad \Xi_t = u_S(1 - \Xi_x) - U, \qquad (2.16a,b)$$

and the force-balance equations (2.6)–(2.7) become

$$p - p_0 + A_R f_R = D_R(Y - 1), \quad \tau_S + pY_x = A_P f_P - D_P \Xi, \qquad (2.17a,b)$$

where $p_0 \equiv 2\Delta T_0/a$. Finally, the equation of motion (2.8) becomes

$$M\dot{U} = F \equiv -\langle \tau_S + pY_x \rangle \equiv -D_P\langle\Xi\rangle. \qquad (2.18)$$

The system above depends on the dimensionless parameters

$$M \equiv \frac{cH\mathcal{M}}{\mu L}, \quad D_R \equiv \frac{2H^3 T_0}{\mu cLa}, \quad D_P \equiv \frac{2HL\Lambda}{\mu c}, \qquad (2.19a,b,c)$$

which are a dimensionless mass per unit area and dimensionless normal and tangential stiffnesses, respectively. Further,

$$A_R f_R(x,t) \equiv \frac{H^2\Delta}{\mu cLa}(T_+ + T_-), \quad A_P f_P(x,t) \equiv \frac{H}{\mu c}(T_+ - T_-), \qquad (2.20a,b)$$

appearing in (2.17a, b), represent scaled normal and tangential forcings, each with dimensionless amplitudes A_R and A_P, and spatial patterns $f_R(x,t)$ and $f_P(x,t)$. Equations (2.20a, b) do not uniquely specify these amplitudes and forcing patterns; we remove this ambiguity later by prescribing the forcing patterns f_R and f_P at the beginnings of §3 and §4, respectively. Our use of P and R subscripts above stems from the significance of the associated quantities in the prograde and retrograde locomotion strategies, as we detail in §2.5 below.

The quantity F appearing in (2.18) represents the net horizontal force on the foot exerted by the fibres. If the muscular forcing has non-zero mean $\langle f_P \rangle \neq 0$, then the locomotor will be driven to accelerate or decelerate relative to the mucus until a uniform horizontal displacement $\Xi_0 \equiv (A_P/D_P)\langle f_P \rangle$ is established, which balances the net tension and the net applied muscular force. These net forces can be absorbed into the system variables by redefining the horizontal displacement and the pattern of muscular forcing as $\Xi - \Xi_0$ and $f_P - \langle f_P \rangle$, respectively. Likewise, any mean normal force $\langle f_R \rangle$ can be removed by suitably redefining the constant p_0 in (2.17a). In other words, we can set $\langle f_R \rangle = \langle f_P \rangle = 0$ without any loss of generality.

Equations (2.15)–(2.16) are the basic ingredients of a model allowing for both normal and tangential displacements of the surface of the foot, driven by two different types of forcings. The main approximations exploited in arriving at these relations are that the mucus layer and the surface of the foot are both shallower than the wavelength of the locomotive waves, that the mucus layer is much thinner than the cavity of the foot and that inertial effects are negligible in both. As a result, we arrive at a lubrication problem inside the mucus layer, with geometrical nonlinearities arising from the kinematic conditions (2.16a, b) and rheological nonlinearity in the Bingham constitutive law (2.15), coupled to linearly elastic forces in the cavity of the foot.

Estimates of the dimensionless parameters can be made as follows. Typical wavelengths and wave speeds for both terrestrial and marine gastropods are $2\pi L \approx 0.01$ m and $c \approx 0.001\,\mathrm{ms}^{-1}$. For the mucus of two species of terrestrial slug, Denny & Gosline (1980)
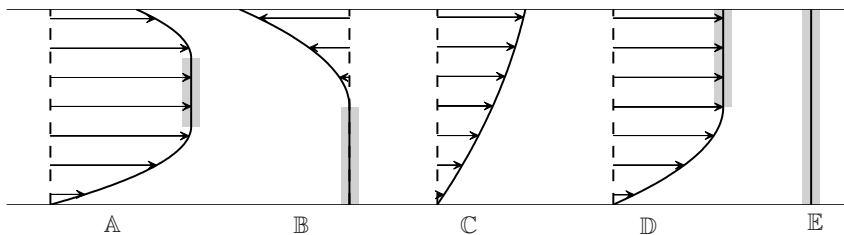
FIGURE 2. Illustration of the velocity profiles of the five flow configurations (2.23). The plug of each profile is indicated by a shaded bar. We have depicted the case $p_x < 0$; for $p_x > 0$, the curvature of the profiles has the opposite sign.

and Ewoldt *et al.* (2007) propose that $\mu \approx 10 - 20\,\mathrm{Pa\,s}$ and $\tau_Y \approx 100 - 200\,\mathrm{Pa}$. Similar values are quoted in the literature for the mucus of marine gastropods (e.g. Holmes *et al.* 2002). Hence, given mucus thicknesses of $H \approx 10^{-5}\,\mathrm{m}$ and $10^{-4}\,\mathrm{m}$ that are characteristic of marine and terrestrial gastropods, respectively (Denny 1981; Lai *et al.* 2011; Holmes *et al.* 2002), we estimate that B can range over the orders of 0.1 to 1. For a typical mass per unit area $\mathcal{M}$ of a few grams per square centimetre, we estimate the dimensionless mass parameter (2.19a) to be of order $M \approx 10^{-5}$. Similar estimates for both B and M follow for the robotic snail of Chan *et al.* (2005). The stiffness and amplitude parameters contained in (2.19b, c) and (2.20a, b) are more difficult to estimate and likely depend significantly on the specific locomotion strategy employed. In §2.5, we instead use the characteristics of each locomotion strategy to suggest appropriate asymptotic limits of these parameters.

2.4. *Flow configurations*

The state of the system is described by $Y(x, t)$, $\Xi(x, t)$ and $U(t)$. The pressure $p(x, t)$ and surface stresses, $\tau_B(x, t)$ and $\tau_S(x, t)$, constitute subsidiary variables that are related to these state variables through the force balances (2.17a, b). Given Y, Ξ and U at a given instant, the velocity field $u(x, y, t)$ can be constructed from an integration of (2.15) subject to the no-slip condition $u(x, 0, t) = 0$ and the surface-stress condition $\tau(x, Y, t) = \tau_S$. As is typical of viscoplastic lubrication problems in general (e.g. Hewitt & Balmforth 2012), this construction is complicated by switches in the constitutive law (2.15b), corresponding to the appearance of rigid plugs or pseudo-plugs, or simply *plugs* for short. Having constructed u, we can use (2.16a, b) and (2.18) to determine the evolution of $Y(x, t)$, $\Xi(x, t)$ and $U(t)$.

By inverting (2.15b), we can express the rate of shear in terms of the shear stress by

$$u_y = \begin{cases} \tau - B\,\mathrm{sgn}(\tau) & |\tau| > B, \\ 0 & |\tau| < B. \end{cases} \tag{2.21}$$

Combining (2.21) with (2.15a), we determine that u has a parabolic vertical profile in fully yielded sections of the flow. Conversely, u is independent of y in the unyielded plugs. The switches in (2.21) occur at $\tau = \pm B$. Given that τ varies linearly from τ_B to τ_S according to (2.15a), at most two such switches can occur at any given location of x. We denote the *yield surfaces* at which these two changes occur by $Y_\pm(x, t)$, where $Y_- < Y_+$. We allow $Y_\pm$ to lie outside the domain of the mucus, corresponding to situations where a plug intersects one of the boundaries. By setting $\tau = \pm B$ in (2.15a), we obtain

$$Y_\pm = \frac{1}{p_x}(-\tau_B \pm B\sigma), \quad \text{where} \quad \sigma \equiv \mathrm{sgn}(p_x). \tag{2.22}$$

Depending on whether $Y_{\pm}$ lie inside or outside the mucus layer, there are five possible flow configurations:

$\mathbb{A}$: $\quad 0 < Y_- < Y_+ < Y,$ $\qquad$ The profile contains a central plug
$\mathbb{B}$: $\quad Y_- < 0$ and $0 < Y_+ < Y,$ $\quad$ A plug is attached to the lower surface
$\mathbb{C}$: $\quad Y_{\pm} < 0$ or $Y_{\pm} > Y,$ $\qquad$ Fluid is yielded across the depth of the layer $\quad$ (2.23)
$\mathbb{D}$: $\quad 0 < Y_- < Y$ and $Y_+ > Y,$ $\quad$ A plug is attached to the surface of the foot
$\mathbb{E}$: $\quad Y_- < 0$ and $Y_+ > Y,$ $\qquad$ A plug spans the depth of the layer

each of which is illustrated in figure 2 for $p_x < 0$. Formulae for u, τ_S and q in terms of p_x and Y for each configuration are given in appendix A. These formulae follow on integration of (2.15) subject to the no-slip conditions at the upper and lower surfaces, given the particular arrangement of yield surfaces associated with each configuration (2.23) (cf. Balmforth *et al.* 2010; Hewitt & Balmforth 2012).

2.5. *Retrograde and prograde locomotion*

Retrograde locomotion is characterized by predominantly normal displacements of the surface of the foot. We configure our general system to model this strategy by assuming that the foot is horizontally stiff, $D_R \gg D_P$. In accordance with (2.17b), the surface of the foot then undergoes negligible tangential deformations independently of the forces exerted on it by the mucus layer, so $\Xi \ll 1$. In turn, (2.16b) then implies that the horizontal velocity of the lower surface of the foot simply equals that of the main body, so $u_S \equiv U$. This simplified retrograde model can be characterized by the three equations

$$\frac{\partial p}{\partial x} + A_R \frac{\partial f_R}{\partial x} = D_R \frac{\partial Y}{\partial x}, \qquad u_S \equiv U, \qquad \frac{\partial Y}{\partial t} + \frac{\partial q}{\partial x} = 0, \qquad (2.24a,b,c)$$

where the former follows from differentiation of (2.17a) with respect to x.

By contrast, prograde locomotion is characterized by predominantly tangential displacements of the surface of the foot. We configure our general system to model this strategy by assuming that the foot is vertically stiff, $D_R \gg D_P$. As implied by (2.17a), the surface of the foot then undergoes negligible normal deformations independently of the forces exerted on it by the mucus layer, so $Y \approx 1$. To further simplify our analysis of the prograde strategy, we adopt a small-amplitude approximation $A_P \ll 1$, under which the nonlinear term in the kinematic surface condition (2.15b) can be neglected. This neglect can be justified by noting that the displacement and velocity of the surface of the foot each scale with the forcing amplitude A_P and hence $\Xi_x u_S \sim A_P^2 \ll u_S \sim A_P$. Such an approximation can be expected to be relevant for gastropod locomotion, where the contractions of the surface of the foot are an order of magnitude smaller than the wavelength of the forcing wave (Lai *et al.* 2011). In summary, our simplified prograde model is characterized by the three equations

$$\tau_S = A_P f_P - D_P \Xi, \qquad Y \equiv 1, \qquad \frac{\partial \Xi}{\partial t} = u_S - U. \qquad (2.25a,b,c)$$

3. Retrograde locomotion

We proceed to analyse the simplified retrograde problem described in §2.5 above with the model forcing pattern $f_R = \sin(x + t)$, corresponding to a sinusoidal wave that travels at unit dimensionless speed in the negative x-direction. To simplify our analysis, we introduce the new spatial coordinate $\xi \equiv x + t$, equivalent to a shift of the system into the frame of the wave. Equations (2.24a, c) then become

$$p_\xi = D Y_\xi - A \cos \xi, \quad Y_t + Y_\xi + q_\xi = 0, \qquad (3.1a,b)$$
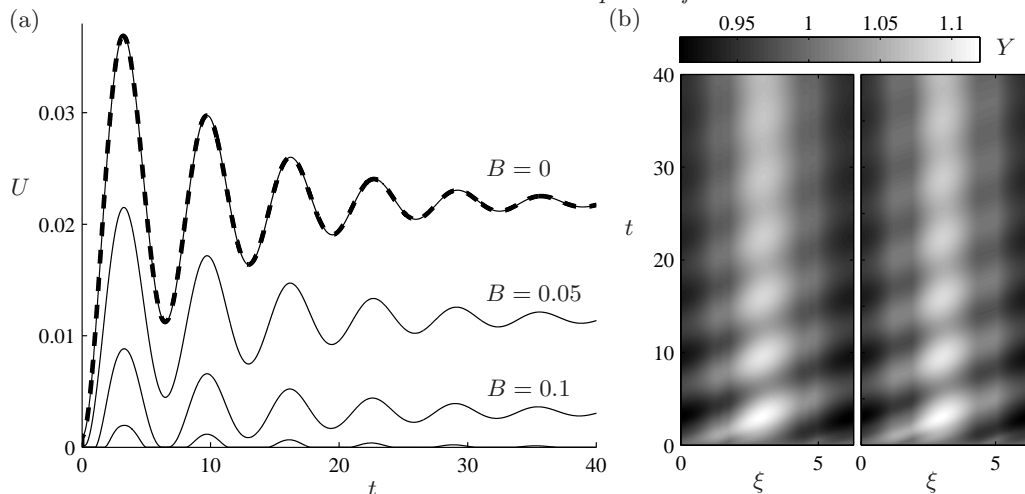
(a)

(b)

FIGURE 3. Solutions to the initial-value problem for retrograde locomotion. Panel (a) shows the evolution of the locomotion velocity $U(t)$ in the case with $A = D = 1$ and $M = 0.1$, for Bingham numbers $B = 0$, 0.05, 0.1 and 0.15 (all thin). The thick, dashed curve shows a solution with $M = 0.001$ and $B = 0$. Panel (b) shows the surface profile $Y(\xi, t)$ as a density on the (ξ, t)-plane, where $\xi \equiv x - t$, for the two solutions in panel (a) with $B = 0.1$ (left) and $B = 0.15$ (right).
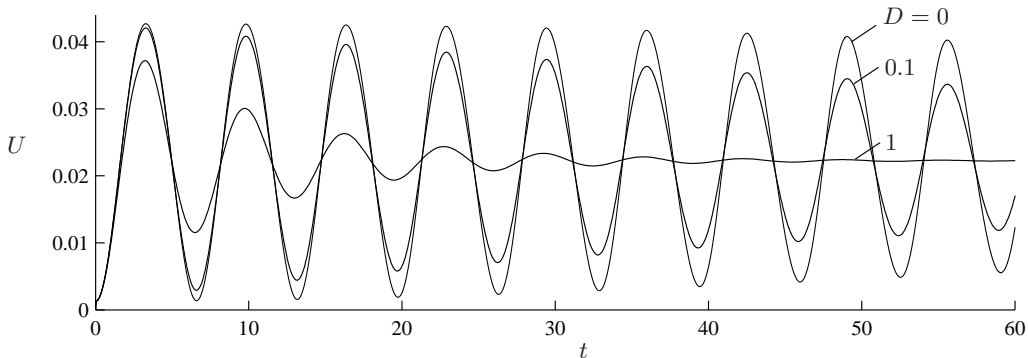
FIGURE 4. Evolution of the locomotion velocity $U(t)$ in the case with $A = 1$, $B = 0$ and $M = 0.1$ for stiffnesses of $D = 0$, 0.1 and 1.

respectively, where we have dropped the R subscript from f_R, D_R and A_R.

3.1. *The initial-value problem*

With Ξ negligible, the state of the system is described by the two remaining state variables $Y(\xi, t)$ and $U(t)$. We begin by solving the system defined by $(2.15a, b)$, (2.18) and $(3.1a, b)$ numerically as an initial-value problem, which is initialized from a state of rest and uniform thickness, $U(0) = 0$ and $Y(\xi, 0) = 1$. To accomplish this, we discretize ξ on a fixed uniform grid and use centred differences to approximate the spatial derivatives. At each time step, we first evaluate p_ξ using $(3.1a)$ and then calculate the flow configuration, flux q and surface stress τ_S using the formulae in appendix A. We then use $(3.1b)$ and (2.18) to compute Y_t and $\dot{U}$, employing quadrature to evaluate period averages, and then advance the system in time using the Matlab integrator `ode15s`.

A complication arises in solving the initial-value problem at the initial instant and at any subsequent instants at which the locomotor is brought to rest, $U = 0$. Specifically, such instants admit the possibility that a rigid plug spans the depth of the mucus layer,
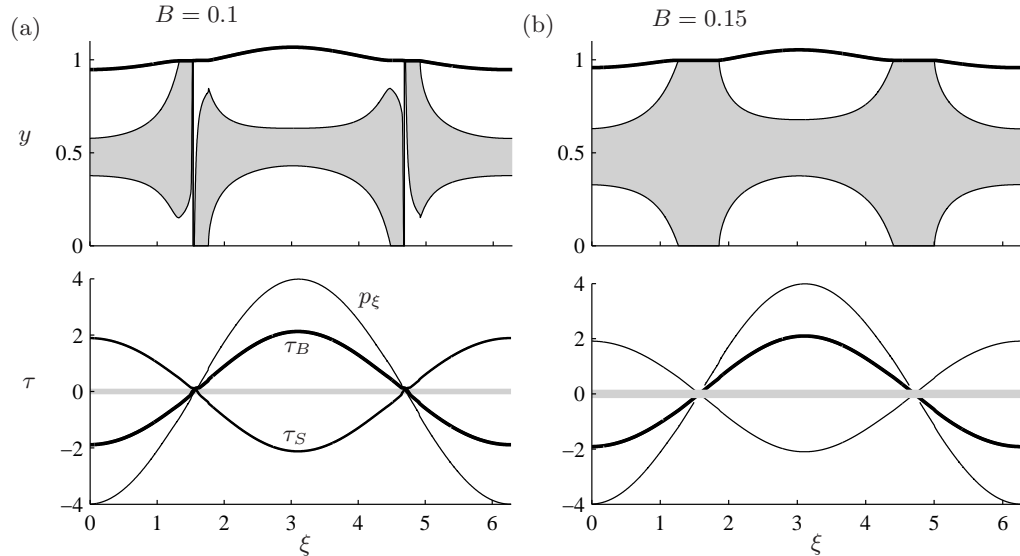
(a) $B = 0.1$ (b) $B = 0.15$

FIGURE 5. Steady-state surface stresses, τ_B and τ_S, yield surfaces $Y_\pm$, and pressure gradient p_ξ, for (a) the locomotive state with $B = 0.1$ and (b) the stationary state with $B = 0.15$. The plugs and stress bands in which the plugs form $|\tau| < B$ have been shaded.

causing the force on the right-hand side of (2.18) to become indeterminate. We postpone a detailed discussion of this issue until §3.2, and first provide an overview of our solutions to build a useful foundation on which to base that discussion.

Figure 3 shows sample solutions for the evolution of $U(t)$ and $Y(\xi, t)$ in the case $A = D = 1$ for a selection of B. Figure 4 displays the effect of varying the stiffness D with $A = 1$ and $M = 0.1$. In each case, the forcing wave begins by generating a perturbation to the surface profile Y that is subsequently overridden and left behind by the wave. As the wave cycles through the periodic domain, the solution oscillates with the period of the forcing wave 2π. As indicated by figure 4, these oscillations are damped if $D > 0$, at a rate which increases with D, and the solutions converge towards states that are steady in the frame of the wave. On the other hand, cases with $D = 0$ exhibit perpetual oscillations that undergo large-time modulations in amplitude, but never decay. The solutions with $M = 0.001$ and $M = 0.1$ are barely distinguishable in figure 3(a), reflecting the existence of a well-defined limit $M \to 0$ in which the inertia of the body vanishes and the position of the locomotor responds instantaneously to the viscous tractions exerted by the mucus layer. Note that the oscillations are therefore not inertial, and are instead associated with the propagation of the forcing wave.

The steady-state distributions of the surface stresses τ_B and τ_S, pressure gradient p_ξ and yield surfaces $Y_\pm$ in the case $B = 0.1$ are shown in figure 5(a). These distributions are representative of states in which the locomotor is moving forwards $U > 0$. The solution contains a pattern of flow configurations (2.23) in the sequence $\mathbb{A}$-$\mathbb{D}$-$\mathbb{C}$-$\mathbb{B}$-$\mathbb{A}$-$\mathbb{B}$-$\mathbb{C}$-$\mathbb{D}$-$\mathbb{A}$ proceeding from $\xi = 0$ to 2π. The thin $\mathbb{C}$ regions that connect the $\mathbb{B}$ and $\mathbb{D}$ regions are essentially indistinguishable in figure 5(a). The composite $\mathbb{B}$-$\mathbb{C}$-$\mathbb{D}$ regions surround the two locations where p_ξ, τ_B and τ_S change sign.

3.2. *Activation and arrest of locomotion*

As noted above, one must exercise caution in solving the initial-value problem if, at some time, $U = 0$. At this juncture, $\mathbb{E}$ regions may form within the mucus layer, causing the
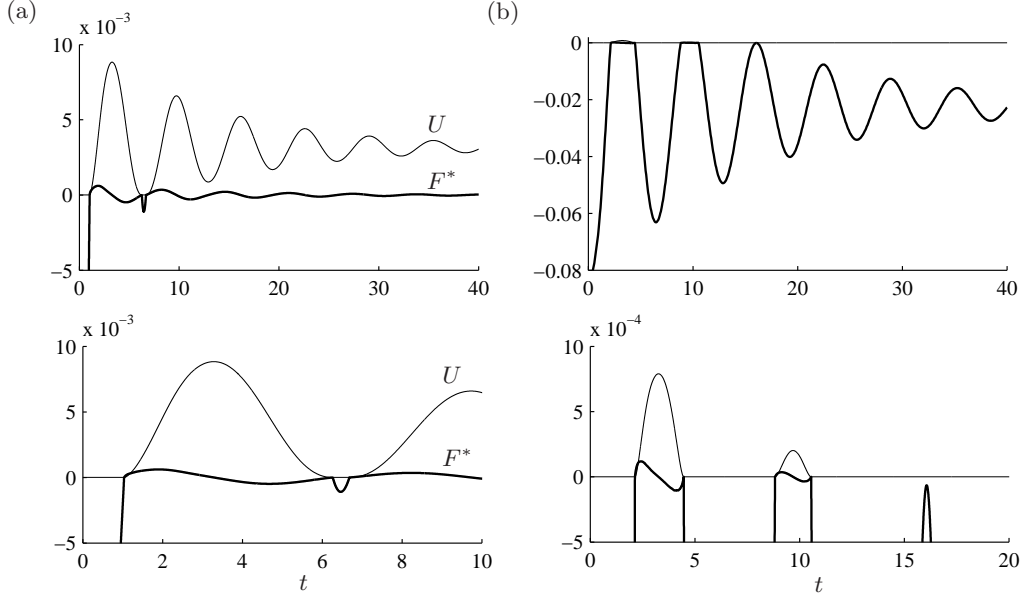
FIGURE 6. Evolution of the activation force $F^*(t)$ (thick), as defined in §3.2, and the locomotion velocity $U(t)$ (thin), for (a) $B = 0.1$ and (b) $B = 0.15$. The lower panels show magnifications of the pinning events wherein $U = 0$ and $F^* < 0$.

shear stress τ to become indeterminate. The resultant force F in (2.18) cannot then be evaluated. In this situation, the locomotor can remain pinned in place for an extended period of time, with (2.18) discarded and replaced by the *pinning condition* $\dot{U} = U = 0$. The flow configurations of the pinned states follow the pattern $\mathbb{A}$-$\mathbb{E}$-$\mathbb{A}$-$\mathbb{E}$-$\mathbb{A}$, as illustrated in figure 5(*b*).

Whenever $U = 0$, the key question to address is whether the drag exerted by the rigid plugs in the $\mathbb{E}$ regions is sufficient to pin the locomotor, or whether the driving force exerted by the foot breaks those rigid plugs and activates locomotion. This question can be answered by examining the state given by the current surface profile together with the limiting locomotion speed $U \to 0^+$, corresponding to that which would be realized if locomotion were to resume. For this hypothetical state, the $\mathbb{E}$ regions are replaced by composite $\mathbb{B}$-$\mathbb{C}$-$\mathbb{D}$ regions and the stresses become determinate. In particular, the surface stress τ_S^* can be constructed in this state and used to evaluate an *activation* force, $F^* \equiv -\langle \tau_S^* + pY_\xi \rangle$. If $F^* > 0$ then (2.18) predicts that $\dot{U} > 0$ and hence the $U \to 0^+$ state is consistent with a successful activation of locomotion. On the other hand, if $F^* < 0$, then (2.18) predicts that $\dot{U} < 0$, implying that the locomotor cannot accelerate away from rest and instead remains pinned.

In all the non-Newtonian examples of the initial-value problems presented in figure 3, the locomotor is pinned briefly at the commencement of each computation, with $U(0) = 0$ and $F^*(0) < 0$ applying in the initial state. For the example with $B = 0.1$, shown in more detail in figure 6(*a*), $F^*(t)$ remains negative until $t \approx 1.2$, whereat the plugs break and locomotion is reactivated. A second, brief interval of pinning occurs around $t \approx 6.3$, but thereafter U remains positive and locomotion continues unimpeded. By $t \approx 40$, the locomotion speed is close to its steady-state value and $F = F^* \to 0$, consistent with a large-time balance of horizontal forces. For $B = 0.15$, shown in figure 6(*b*), the evolutions of U and F^* are qualitatively similar to the case $B = 0.1$ until $t \approx 6$. After this time, however, the locomotion becomes punctuated by further intervals of pinning. The last
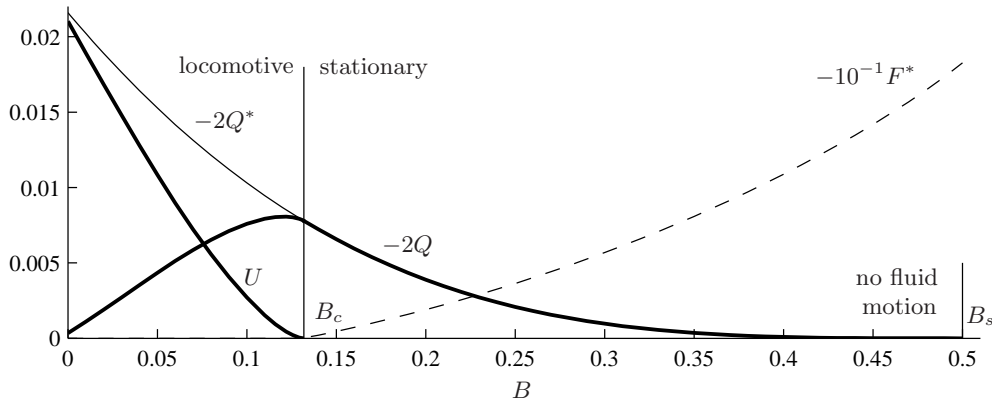
FIGURE 7. Steady-state locomotion velocity U and flux Q plotted against Bingham number B for $A = D = 1$. The thinner curve shows the flux Q^* that would result if $U = 0$ were imposed for $B < B_c$, as discussed in §3.4.

such interval, which commences at $t \approx 11$, persists indefinitely, with F^* converging towards a negative value at large times. Despite the absence of locomotion during this final interval, the surface of the foot converges towards a shape that is steady in the frame of the wave, as illustrated by figure 3(b), corresponding to a pattern of displacements that continue to propagate in the frame of the laboratory. By comparing the two density plots of figure 3(b), we see that the evolution of Y is essentially identical to that of the locomotive case $B = 0.1$, and is therefore largely insensitive to the horizontal translation of the surface of the foot.

3.3. Steady locomotive states

The large-time steady states can be constructed more directly by considering the steady forms of (3.1a, b), which after integration of the first of these, imply

$$Y + q = 1 + Q, \qquad \langle \tau_S + pY_\xi \rangle = 0, \qquad (3.2a,b)$$

where $Q = \langle q \rangle$ is the net flux of mucus. These equations, in conjunction with $\langle Y \rangle = 1$, define an eigenvalue problem for $Y(\xi)$ in which Q and U play the role of eigenvalues. We solve this problem numerically using a Newton-Raphson iteration scheme in which the spatial derivatives and integrals are approximated in the manner described in our solution to the initial-value problem in §3.1.

Figure 7 shows the steady locomotion speed U as a function of the yield stress B for $A = D = 1$. As suggested by our solutions to the initial-value problem shown in figure 3(a), U decreases monotonically with B from the Newtonian case $B = 0$, before vanishing at a critical value $B_c(A, D)$. Figure 8 illustrates how B_c increases with both A and D.

For $B > B_c$, we solve for the stationary states with $U = 0$ by modifying our eigenvalue solver. Specifically, we abandon the shear-stress constraint (3.2b) and the eigenvalue U and instead impose the pinning condition $U = 0$. We confirm the consistency of these stationary states by evaluating the activation force F^* and verifying that it is negative for $B > B_c$, as illustrated by the dashed curve in figure 7.

We explore the onset of steady locomotion as B is reduced from B_c in more detail by considering the asymptotic limit of small amplitude and stiffness. By performing a
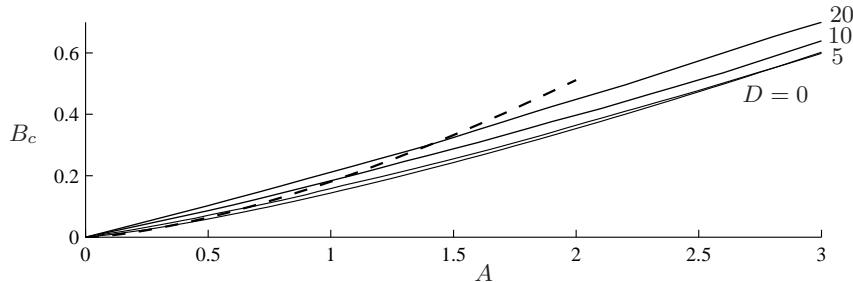
FIGURE 8. Critical Bingham number $B_c(A, D)$ above which locomotion is arrested as a function of amplitude A for stiffnesses of $D = 0$, 5, 10 and 20. The small-A, small-D analytical approximation for B_c determined from (3.3) is shown as a dashed curve.
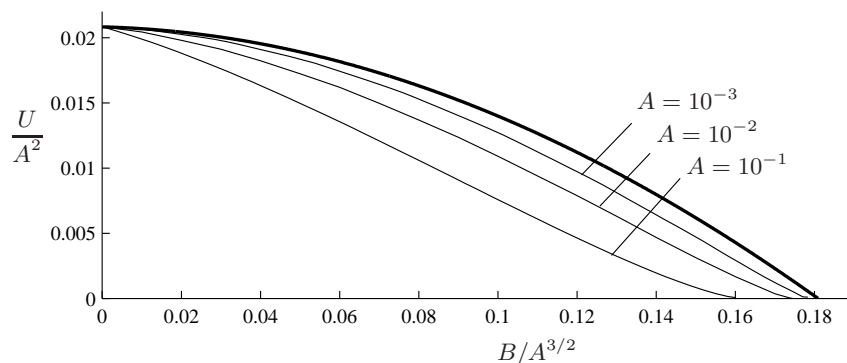

FIGURE 9. Scaled locomotion speeds U/A^2 plotted against the scaled Bingham number $B/A^{3/2}$ for $D = 0$ and $A = 10^{-1}$, 10^{-2} and 10^{-3} (all thin). The small-amplitude, small-stiffness approximation (3.3) in the case $A = 10^{-3}$ is shown as a thick curve.

perturbation analysis in this limit (see appendix B), we determine the approximation

$$U \left[1 - \frac{2B}{\pi A} \log\left(\frac{BU}{A^2}\right)\right] \sim \frac{1}{48}A^2 - \frac{2B^2}{\pi A} \qquad (A \ll 1, D \to 0), \tag{3.3}$$

where $B \le B_c(A, 0) = \left(\pi A^3/96\right)^{1/2}$. In the Newtonian case ($B = 0$), (3.3) implies that $U \sim A^2/48$, which is consistent with the small-amplitude results of Katz (1974). For $B > 0$, the second term on the right-hand side of (3.3) provides a first-order correction to the Newtonian result. Specifically, the correction originates from the yield stress in the weakly yielded $\mathbb{B}$ and $\mathbb{D}$ regions that surround the two locations where p_ξ changes sign. Locomotion is thus most strongly constrained by the yield stress in the near-rigid plugs that are close to spanning the depth of the mucus layer. The logarithmic term in (3.3) originates from the global contribution of the yield stress in the strongly yielded $\mathbb{A}$ regions that occupy the majority of the mucus layer. The prediction for U implied by (3.3) is compared with numerical solutions in figure 9.

3.4. *Generation of flux*

As shown in figure 7, both the stationary and locomotive states generate a flux $Q < 0$ in the direction opposite to that of locomotion. The magnitude of Q is seen to increase with B from a finite value at $B = 0$ towards a maximum near B_c. Notably, despite the existence of static fluid in the $\mathbb{E}$ regions for $B > B_c$, the yielded fluid in the $\mathbb{A}$ regions
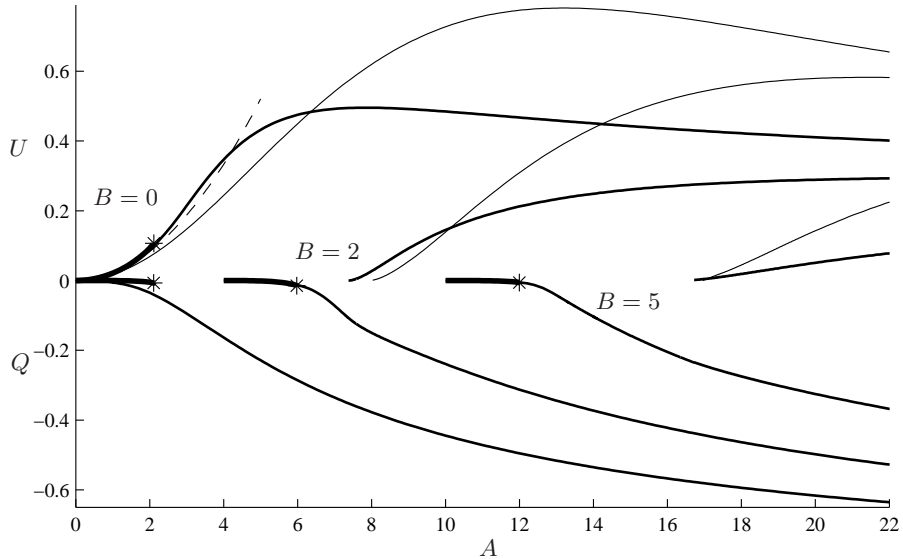
FIGURE 10. Locomotion speed U plotted against amplitude A for $B = 0$, 2 and 5 and stiffnesses $D = 0$ (thick), $D = 1$ (mid-weight) and $D = 5$ (thin). The small-amplitude result (3.3) is shown as a dashed curve in the case $B = 0$. The lower part of the plot shows the net flux Q for the same values of B and $D = 0$ (thick) and 1 (mid-weight). The flux Q vanishes and is not plotted for $B < B_s$, where B_s is given by (3.4). For the cases with $D = 0$, the critical amplitude A^* at which a shock first forms is indicated by a star.

are still able to deliver a net flux. This is possible because the yield surfaces $Y_\pm$ change position as the forcing wave propagates, so fluid crosses the borders of the $\mathbb{E}$ regions.

In the stationary states ($B > B_c$), the system becomes equivalent to a kind of peristaltic pump (e.g. Shapiro *et al.* 1969). Indeed, if we artificially impose $U = 0$ and ignore (3.2*b*), then we recover a two-dimensional model of peristaltic pumping that is related to the axisymmetric problems of Vajravelu *et al.* (2005) and Takagi (2009). The continuation of the flux Q for $B < B_c$ with $U = 0$ imposed is shown as a thin curve in figure 7, where it is seen to continue increasing as B is reduced, obtaining a maximum in the Newtonian case. By contrast, the flux Q of the locomotive states soon begins to decrease as B reduces below B_c. This occurs because the translation of the upper surface opposes the peristalsis. For gastropods, the generation of a backward flux is wasteful because it demands an enhancement of mucus production.

There is yet a further threshold $B_s(A)$ above which the net transport of flux Q vanishes entirely. Beyond this threshold, the forces exerted by the foot are insufficient to yield the fluid anywhere. This occurs critically when the yield surfaces $Y_\pm$ lie entirely outside the mucus layer, so $\max_\xi(Y_-) = 0$. Combining this criterion with (2.22), we deduce that $2B_s = \max_\xi |p_\xi|$ and hence

$$B_s = \tfrac{1}{2}A, \tag{3.4}$$

where we have used (3.1*b*) to substitute for p_ξ and noted that $Y \equiv 1$ in the static state. Unlike B_c, (3.4) is independent of D, which follows from the fact that the elastic force is identically zero when the foot suffers no deformation.
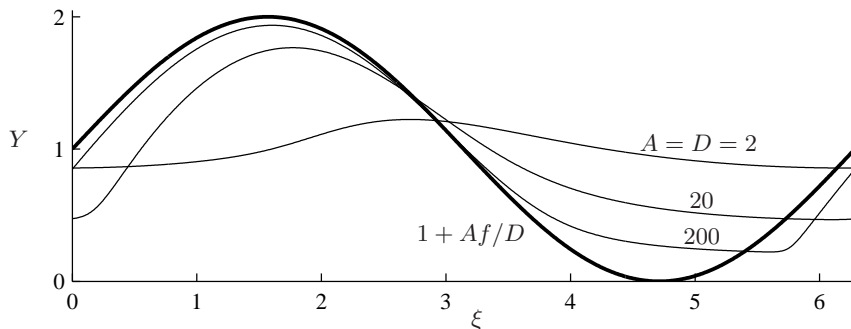
FIGURE 11. Steady-state surface profiles Y for $B = 0$ and $A = D = 2, 20$, and 200, illustrating the convergence towards the large-amplitude, large-stiffness asymptote (3.5) (thick).

3.5. *Effects of forcing amplitude and stiffness*

Figure 10 shows the locomotion speed U and net flux Q as functions of the forcing amplitude A for a selection of Bingham numbers $B = 0, 2$ and 5, and stiffnesses $D = 0, 1$ and 5. In the Newtonian case ($B = 0$) with $D = 1$, U increases approximately quadratically with A at small forcing amplitudes in accord with (3.3), which is plotted as a dashed curve. However, this trend does not continue for $A \gtrsim 2$. Instead, U reaches a maximum at $A \approx 8$ and then proceeds to decrease. The eventual reduction of U is due to the enhancement of the viscous drag in the thinnest part of the mucus layer, which becomes increasingly constricted at large A as the foot is pressed closer to the base (Balmforth *et al.* 2010).

Comparison between the Newtonian ($B = 0$) cases of $D = 1$ and $D = 5$ in figure 10 shows that an increase in D leads to a reduction in U at sufficiently small amplitudes $A \lesssim 6$. This reflects the fact that the elastic force resists the vertical deformations that drive locomotion. However, given a sufficiently large forcing amplitude $A \gtrsim 6$, increasing D leads to a larger locomotion velocity U. This occurs because the resistance to deformation provided by the elastic force eventually opposes the localized constriction of the mucus layer that provides the dominant resistance to locomotion at large A.

For large stiffnesses ($D \gg 1$), it is clear from (3.1a) that a correspondingly large amplitude $A \sim D$ is needed for any significant locomotion to be generated. If $A \sim D \gg 1$, then the leading-order balance in (3.1a) is between the elastic and muscular terms on the right-hand side, implying that the forcing in this limit directly dictates the displacement of the foot according to

$$Y \sim 1 + (A/D)f \qquad (A \sim D \gg 1). \tag{3.5}$$

The convergence of Y towards the asymptote (3.5) is illustrated in figure 11, where we have plotted Y for increasing values of $A = D$ in the case $B = 0$. Note that if $A \geq D$, then (3.5) predicts that Y intersects the lower boundary in the thinnest region of the mucus layer, so (3.5) cannot apply in these regions. Instead, p_ξ remains significant in (3.1c) and its intervention prevents the intersection of the surfaces, as is seen to occur near $\xi = 3\pi/2$ in figure 11.

With a perfectly flexible foot ($D = 0$), U is essentially the same as the case $D = 1$ for $A \lesssim 2$, as indicated by the plots of figure 10. However, as A increases towards a critical value, given by $A^*(B) = A^*(0) \approx 2.2$ in the Newtonian case, the surface profile Y develops a discontinuous gradient at the location of greatest forcing $\xi = \pi$, and no smooth solutions exist at larger forcing amplitudes. The thick curves representing $D = 0$ in figure 10 have correspondingly been terminated at A^*. Given a finite stiffness $D > 0$,
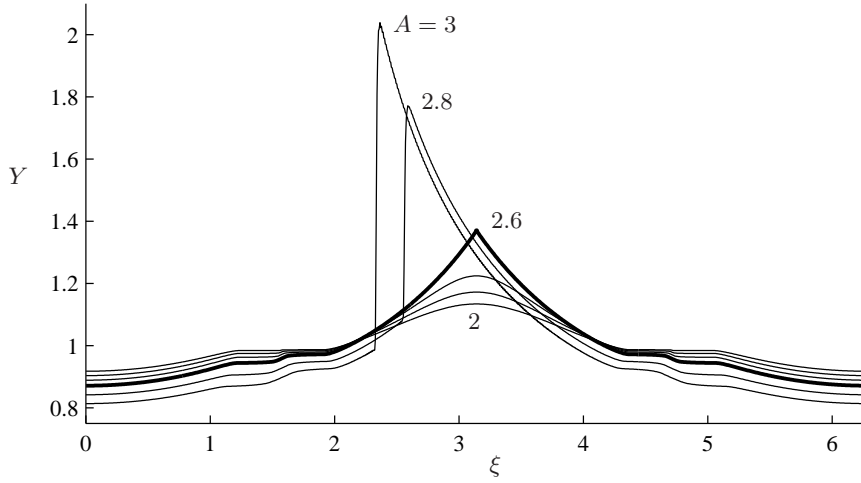
FIGURE 12. Steady-state thickness profiles Y in the small-stiffness case $D = 0.01$ with $B = 0.3$ for $A = 2$, 2.2, 2.4, 2.6, 2.8 and 3. The case with the critical amplitude $A^*(B) = A^*(0.3) \approx 2.6$ at which a shock forms in the case $D = 0$ is shown as a thick curve.

however, the surface maintains a smooth profile as A is increased beyond A^*, but develops a steep shock, as illustrated for $B = 0.3$ in figure 12. Here, we have set $D = 0.01$ and plotted $Y(\xi)$ for several values of A that straddle the critical amplitude $A^*(0.3) \approx 2.6$. The sudden loss of symmetry about $\xi = \pi$ as A increases beyond A^* is a notable feature. As illustrated by the stars in figure 10, $A^*(B)$ increases with B, with the approximate relationship $A^* \approx 2(B + 1)$. For $B \gtrsim 0.9$, the critical amplitudes A^* occur within the branch of stationary states, so there are no smooth locomotive states in these cases if $D = 0$.

4. Prograde locomotion

The simplified model of prograde locomotion problem described in §2.5 allows for tangential displacements of the foot surface but precludes any vertical deformations. With this simplified model, it is possible to rescale Ξ, U, u, p and τ by A_P, such as to eliminate A_P from the problem and introduce a rescaled Bingham number $B' \equiv B/A_P$. Equivalently, we set $A_P = 1$ and use B to denote B' throughout this section. We also drop the P subscript from D_P and f_P.

With $Y \equiv 1$, the state of the system is described by Ξ and U only. On transforming the coordinate system into the frame of the wave (ξ, t), where $\xi \equiv x - t$, equations (2.16a), (2.25a, c) and (2.18) give

$$q = Q(t), \quad \tau_S = f - D\Xi, \quad \Xi_t = u_S - U + \Xi_\xi, \quad M\dot{U} = \langle \tau_S \rangle = -D\langle \Xi \rangle, \quad (4.1a,b,c,d)$$
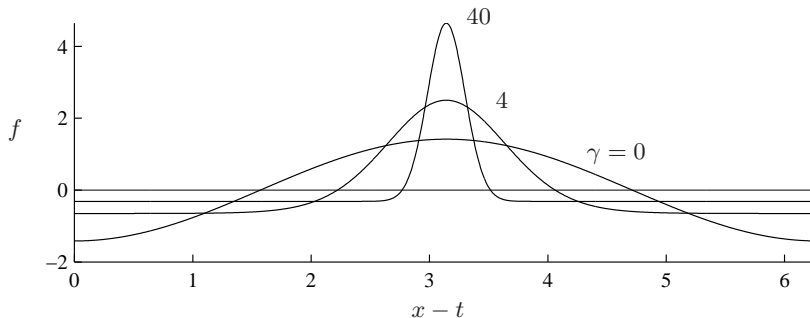
respectively.Notably, (4.1a) implies that the flux q is spatially uniform at all times.

For the purpose of illustration, we consider the model forcing pattern

$$f(\xi) = \frac{g - \langle g \rangle}{\left[\langle g^2 \rangle - \langle g \rangle^2 \right]^{1/2}}, \quad \text{where} \quad g \equiv e^{-\gamma \cos \xi} \quad (4.2)$$

and $\gamma \geq 0$ is a *forcing parameter*. The pattern (4.2) satisfies the property $\langle f \rangle = 0$ and has been normalized so that $\langle f^2 \rangle = 1$. As shown in figure 13, the limiting case $\gamma \to 0$

FIGURE 13. Prograde forcing pattern (4.2) for $\gamma = 0, 4$ and 40.

corresponds to a sinusoidal forcing pattern $f = -\sqrt{2}\cos\xi$. For $\gamma > 0$, the forwards-forced region is of smaller horizontal extent than the backwards-forced region, but attains a greater magnitude.

4.1. *The Newtonian problem*

In the Newtonian case $B = 0$, the lubrication equation (A 2) simplifies to

$$\tau_S = u_S + \tfrac{1}{2}p_\xi \quad \text{and hence} \quad \langle\tau_S\rangle = \langle u_S\rangle. \tag{4.3a,b}$$

Taking the period averages of $(4.1b, c, d)$, we obtain

$$\langle\tau_S\rangle = -DX, \quad \langle u_S\rangle = U + \dot{X}, \quad M\dot{U} = DX, \tag{4.4a,b,c}$$

respectively, where $X(t) \equiv \langle\Xi\rangle$ is the net horizontal displacement of the lower surface of the foot. By combining $(4.3b)$ and $(4.4a, b, c)$, we determine the evolution equation

$$M(\ddot{U} + D\dot{U}) + DU = 0, \tag{4.5}$$

which shows that U evolves as a damped linear oscillator. With the initial condition $\Xi(\xi, 0) = U(0) = 0$, corresponding to an initially unperturbed state, (4.5) implies that $U = 0$ for all time, so the locomotor remains stationary. Even if the system were initialized in some other fashion, (4.5) still implies that $U \to 0$ as $t \to \infty$. Steady locomotion with this prograde strategy is therefore impossible with Newtonian mucus. This result contradicts Katz's (1974) analysis of the low-amplitude biharmonic problem, which demonstrates that prograde locomotion is feasible with Newtonian fluid (see also Tuck 1968). The discrepancy arises because of our linearization of the horizontal kinematic condition in $(2.12b)$ performed in §2.5. Though appropriate for gastropods, this approximation rules out a weak form of locomotion analogous to steady streaming or Stokes drift.

Note that the frequency of the oscillations $[(MD)^{-1} - 1/4]^{1/2}$ implied by (4.5) is set by M and D, revealing them to be inertio-elastic, and overdamped for $DM > 4$. The transient dynamics are therefore different from the retrograde case considered in §3.1, where the oscillations of the initial-value problem were found to be associated with the propagation of the forcing wave.

4.2. *The viscoplastic initial-value problem*

For viscoplastic cases $(B > 0)$, we again consider the evolution of the system from an unperturbed initial state with $\Xi(\xi, 0) = U(0) = 0$. We solve the initial-value problem described by $(2.15a, b)$ and $(4.1a, b, c, d)$ numerically by, once again, discretizing ξ on a fixed uniform grid and employing centred differences to approximate spatial derivatives.
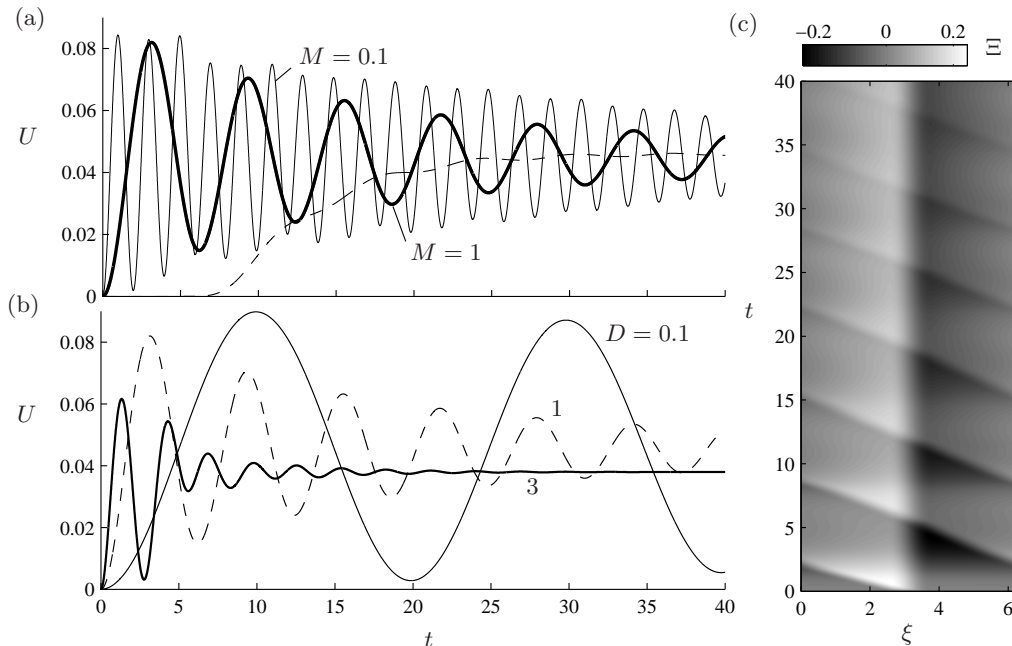
FIGURE 14. Locomotion speed $U(t)$ against time for $\gamma = 4$ and $B = 0.6$ in initial-value computations with (a) $D = 1$, $M = 1$ (thick) and $M = 0.1$ (thin), and (b) $M = 1$ and $D = 0.1$ (thin), 1 (dashed) and 3 (thick). Panel (c) shows the tangential foot displacement Ξ as a density on the (ξ, t)-plane in the case with $M = D = 1$. In (a), the dashed line shows the result of a computation with $M = D = 1$ in which the forcing is switched on more gradually by multiplying the forcing pattern f by the time-dependent function $\tanh^2(t/10)$.

At the beginning of each time step, p_ξ and Q are unknown and must be determined such that (4.1a) is satisfied at each grid point, with u constructed using the formulae in appendix A, together with the continuity condition, $\langle p_\xi \rangle = 0$. To accomplish this, we use a Newton-Raphson scheme in which p_ξ and Q are iterated from their values in the previous time step. Having obtained p_ξ and u, we use (4.1c, d) to integrate Ξ and U forwards in time.

As in the retrograde problem, there is a complication in solving the initial-value problem whenever $\mathbb{E}$ regions appear in the mucus layer. The main consequence here is that p_ξ becomes indeterminate over these regions and the constraint $\langle p_\xi \rangle = 0$ ceases to be applicable. Instead, (4.1a) and the stagnancy of the flow in the $\mathbb{E}$ regions together imply that $q = Q = 0$. This no-flux condition can be used to solve for p_ξ outside the rigid plugs, thereby providing u_S and the means to evolve Ξ using (4.1b). Over the rigid plugs themselves, the displacement of the foot surface is frozen in time, so $\Xi_t = 0$.

Sample numerical solutions to the initial-value problem with $\gamma = 4$ and $B = 0.6$ are shown in figure 14. Panel (a) shows computations with the two different dimensionless masses per unit area of $M = 0.1$ and 1, for fixed $D = 1$. Panel (b) shows cases with stiffnesses of $D = 0.1, 1$ and 3, for fixed $M = 1$. As in the retrograde problem, the switch-on of the muscular forcing at $t = 0$ generates a disturbance in Y that decomposes into a component that is carried along in the wave frame and a component that propagates with a different speed. As illustrated in figure 14(c), this component decays as it recirculates through the domain. The system eventually converges towards a state that is steady in the frame of the wave.
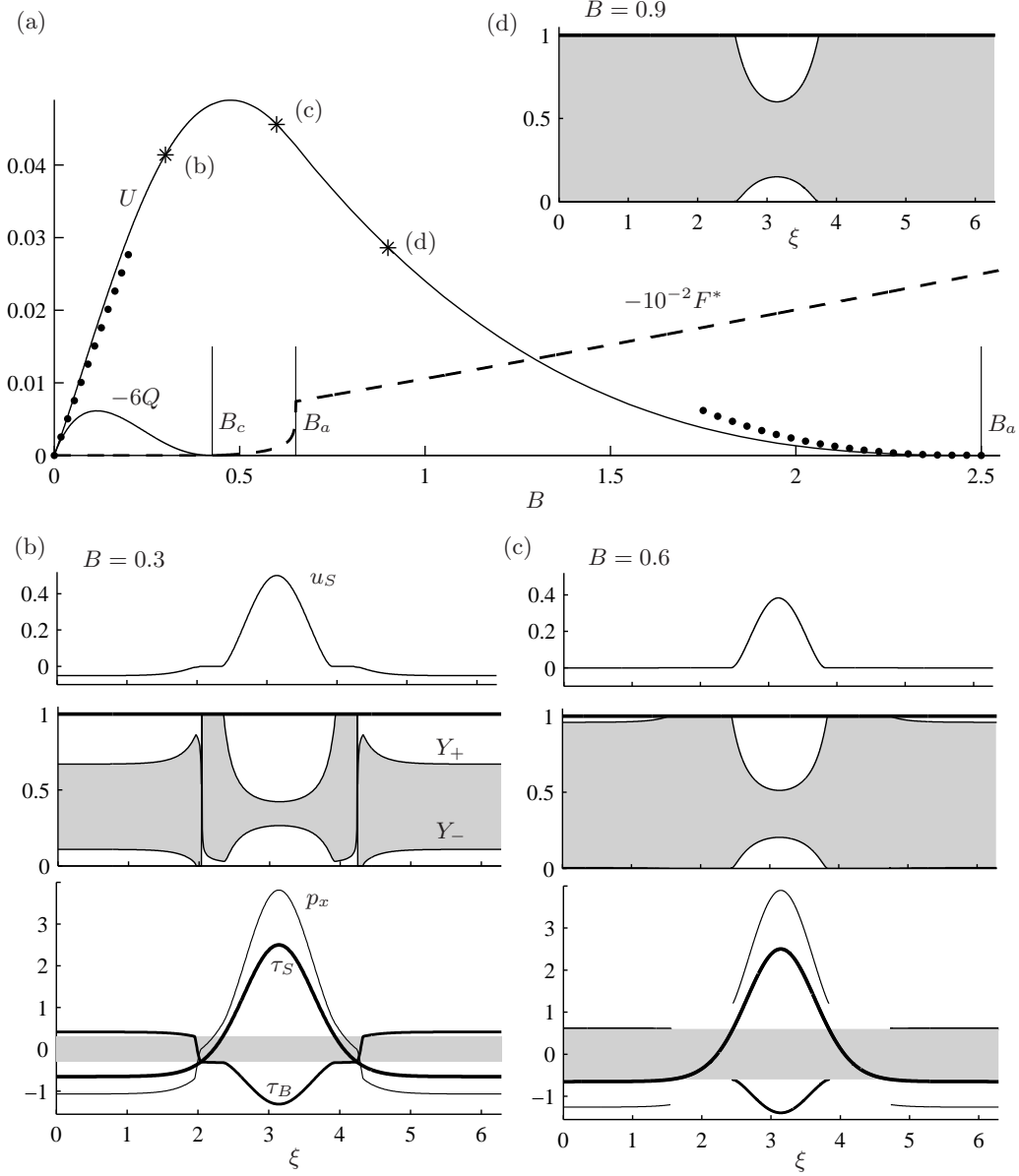
FIGURE 15. Steady-state solutions for prograde locomotion for $\gamma = 4$ and $D = 0$. Panel (a) shows the locomotion speed U and flux Q as a function of B. The dotted curves show asymptotic approximations for $B \ll 1$ and $B \to B_s \approx 2.5$, given by (4.8) and (4.14), respectively. The force F^*, defined in (4.10), indicating when flux is generated is shown as a dashed curve, and the vertical lines mark the critical values, B_c, B_s and B_a. Panels (b)–(d) show the yield surfaces $Y_\pm$ for $B = 0.3$, 0.6 and 0.9, respectively, the locations of which are shown by stars in (a). The distributions of u_S, p_ξ, τ_B and τ_S are also plotted in (b) and (c).

The most notable characteristic of the non-Newtonian solutions to the initial-value problem compared with the Newtonian solutions is that the large-time steady-state values of U are non-zero. The yield stress therefore generates locomotion. One can understand this result by noting that the yield stress acts to impede flow within the fluid layer,

thereby restricting the foot speed u_S at each x-location. Therefore, if $f(\xi)$ contains a backwards-forced region that is longer but weaker than the forwards-forced region, such as that provided by (4.2) with $\gamma > 0$, then the yield stress will block flow preferentially in the backwards direction. The resulting asymmetry implies that $U = \langle u_S \rangle > 0$, so locomotion is activated in the forwards direction, despite the vanishing of the net driving force, $\langle \tau_S \rangle = 0$. Indeed, if γ is sufficiently large then it is possible for the yield stress to stop backwards motions of the foot surface entirely, so $u_S \geq 0$; an example of such a state is shown later in figure 15(d).

Figure 14(b) illustrates how the stiffness D controls the convergence of the system towards the steady state in a manner that is similar to the retrograde problem. Unlike that problem, however, the frequency of the oscillations is dependent on D and M, which identifies them as inertio-elastic. As indicated in our discussion of the Newtonian problem in §4.1, the frequency of the oscillations diverge in the limit $M \to 0$, which, in view of our small estimate of $M \approx 10^{-5}$ given in §2.3, should be applicable to the biological setting. However, gastropods do not display any significant oscillation as they initiate locomotion, implying a disparity between the predictions of our model and the biological observations, indicating a possible limitation of our idealized model. The addition of some other physical effect may be needed in order to prevent the unphysical divergence of the oscillation frequency in the limit $M \to 0$ and to explain the prediction of transient oscillations for parameter settings relevant to gastropods. One possibility is that the viscous traction in the foot cavity, which we have neglected, may intervene to prevent any rapid oscillation of the cavity. Another possibility, identified in the Newtonian case in §4.1 above, is that the evolution is overdamped. However, this seems unlikely if $M \approx 10^{-5}$. A further possibility, which appears more plausible, is that the oscillations in our computations are an artefact of our imposition of an instantaneous switch-on of the forcing wave at $t = 0$, leading to an abrupt start to the system that is physically unrealistic. By computing solutions to the initial-value problem with a forcing whose amplitude is gradually ramped up over a time longer than the period of oscillation, we have verified that the oscillatory transients are suppressed. An example of such a computation, obtained by multiplying f_P by a time-dependent function $\tanh^2(t/10)$, is shown as a dashed line in figure 14(a).

4.3. *Steady locomotive states*

We can compute the steady states more directly by considering the steady forms of (4.1b,d), namely,

$$\Xi_\xi = U - u_S, \quad \langle \tau_S \rangle = -D\langle \Xi \rangle = 0. \qquad (4.6a,b)$$

In cases where the steady state contains no $\mathbb{E}$ regions, p_ξ is determinate over the full domain and (4.1a,b), (4.6a,b) and $\langle p_\xi \rangle = 0$ constitute an algebraic problem for p_ξ, Ξ, Q and U. We solve this problem using a similar discretization of ξ and Newton-Raphson iteration to that described in §4.2, but including (4.6a,b) as objective functions and Ξ as an iteration variable. To compute the solution in flux-less cases, we impose $Q = 0$ and abandon the constraint $\langle p_\xi \rangle = 0$.

Figure 15 displays steady-state solutions for $\gamma = 4$ and $D = 0$. Note that, although we do not expect the system to converge towards a large-time steady state if $D = 0$, these solutions are typical of small but finite stiffness. As shown by panel (a) of this figure, the steady-state locomotion velocity U increases with B from zero in the Newtonian case up to a maximum $U_{\text{opt}}(\gamma, D) \equiv \max_B(U) \approx 0.049$ at $B = B_{\text{opt}} \approx 0.47$. Thereafter, U decreases and eventually vanishes at the critical value $B = B_s \approx 2.5$, corresponding to the cessation of all fluid motion. Thus, although the yield stress is responsible for

activating locomotion by suppressing backward motion, its impedance of forward fluid motion ultimately stops locomotion.

The corresponding flux Q, also shown in figure 15(a), initially decreases from zero as B is increased from the Newtonian case, implying the activation of a backwards transport of mucus. Before the fastest locomotion speeds are achieved, however, the magnitude of the flux reaches a maximum and then decreases back to zero, vanishing beyond a critical value $B_c \approx 0.43$.

Figures 15(b)-(d) show the yield surfaces $Y_\pm$ for three different Bingham numbers $B = 0.3, 0.6$, and 0.9. The corresponding distributions of the surface velocity u_S, pressure gradient p_ξ, and surface stresses τ_B and τ_S, are also shown for the first two cases. In the flux-generating case $B = 0.3 < B_c$, the flow configurations follow the pattern $\mathbb{A}$-$\mathbb{B}$-$\mathbb{C}$-$\mathbb{D}$-$\mathbb{A}$-$\mathbb{D}$-$\mathbb{C}$-$\mathbb{B}$-$\mathbb{A}$. As the yield stress increases beyond B_c, however, the flux becomes blocked once the $\mathbb{B}$-$\mathbb{C}$-$\mathbb{D}$ regions fuse into $\mathbb{E}$ regions. As shown in figure 15(c) for the case $B = 0.6 > B_c$, the flow configurations then follow the sequence $\mathbb{A}$-$\mathbb{E}$-$\mathbb{A}$-$\mathbb{E}$-$\mathbb{A}$. At yet larger yield stresses $B > B_a \approx 0.65$, the flow configuration changes a third time due to the disappearance of the backwards-forced $\mathbb{A}$ region. Only the forwards-forced $\mathbb{A}$ region then remains, as illustrated by the case $B = 0.9 > B_a$ shown in figure 15(d).

4.4. *Activation of locomotion*

We explore the activation of locomotion in more detail by analysing the near-Newtonian limit $B \ll 1$. In this limit, the flow pattern is dominated by $\mathbb{A}$ regions that are separated by narrow combinations of $\mathbb{B}$-$\mathbb{C}$-$\mathbb{D}$ regions, each surrounding the two locations where p_ξ changes sign. Over the $\mathbb{A}$ regions, the formulae for the flow profiles (A 2) and (A 1), with (2.22) used to eliminate $Y_\pm$, can be simplified in the limit $B \ll 1$, to give

$$Q \sim \frac{\tau_S}{2} - \frac{p_\xi}{3} + \left(\frac{1}{2} - \frac{\tau_S{}^2}{p_\xi^2} \right) B\sigma, \qquad u_S \sim \tau_S - \frac{p_\xi}{2} + \left(1 - \frac{2\tau_S}{p_\xi} \right) B\sigma, \quad (4.7a,b)$$

where $\sigma \equiv \mathrm{sgn}(p_\xi)$, and we have omitted terms of $O(B^2)$. In view of the steady-state condition $\langle \tau_S \rangle = 0$, the spatial averages of (4.7a,b) imply that U and Q are each $O(B)$. In turn, it then follows from (4.7a) that $p_\xi = 3\tau_S/2 + O(B)$. Using this expression to evaluate p_ξ in the first-order terms in (4.7a,b) and then taking the period averages of these equations, we deduce that

$$U \sim -\tfrac{1}{3}B\langle\sigma\rangle + O(B^2), \qquad Q \sim \tfrac{1}{18}B\langle\sigma\rangle + O(B^2), \qquad (4.8a,b)$$

where $\sigma \sim \mathrm{sgn}(\tau_S)$ represents the direction in which the yield stress opposes motion at each location of ξ.

Finally, we determine τ_S by substituting the leading-order approximation $u_S \sim -\Xi_\xi \sim \tau_S/4$, obtained by combining (4.6a) and (4.7), into the ξ-derivative of (4.1c) to obtain

$$\tau_S{}' - \tfrac{1}{4}D\tau_S = f', \qquad (4.9)$$

where we have used primes to denote $\mathrm{d}/\mathrm{d}\xi$, which can be reduced to quadrature. For $D = 0$, this final step is unnecessary because (4.1b) implies directly that $\tau_S = f$, so $\langle\sigma\rangle = \langle f \rangle$. For our illustrative forcing patterns (4.2), we therefore have $\langle\sigma\rangle < 0$ if $\gamma > 0$, implying that the yield stress suppresses more flow over the wider backwards-forced regions than the narrower forwards-forced regions. Also, $\langle\sigma\rangle$ increases with γ, indicating that larger values of γ are more favourable for generating locomotion in the limit $B \ll 1$. The asymptotes (4.8a, b) are shown as dotted curves in figure 15.
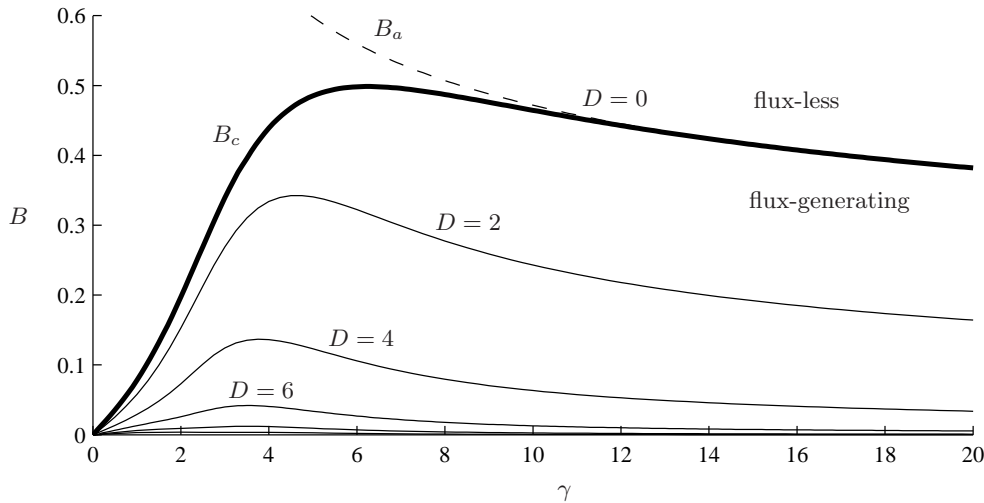
FIGURE 16. Critical Bingham number above which flux generation is arrested $B_c(\gamma, D)$ plotted as a function of γ for stiffnesses of $D = 0, 2, 4, 6, 8$ and 10. In the case $D = 0$, the flux-less and flux-generating regions of parameter space are indicated, and the critical Bingham number $B_a(\gamma, D)$ at which all backwards motions of the foot surface are first arrested by the yield stress is shown as a dashed curve.

4.5. *Blockage of flux*

For $B > B_c$, the flux q vanishes because of the appearance of rigid plugs that span the depth of the mucus layer. The threshold $B_c(\gamma, D)$ can be conveniently computed by considering the force balance on steady states with the no-flux condition $q = 0$ imposed. As indicated by comparing the cases with $B = 0.3 < B_c \approx 0.34$ and that of $B = 0.6 > B_c$ in figure 15(*b*), the breaking of the rigid plugs as B is decreased from B_c corresponds to the replacement of the $\mathbb{E}$ regions by $\mathbb{D}$ regions. The net force associated with breaking the rigid plugs, $F^* = \langle \tau_S \rangle = \langle \tau_B \rangle$, can be split into two parts, $F^* = F_{\mathbb{A}} + F_{\mathbb{D}}$, which represent the contributions to F^* from the $\mathbb{A}$ and $\mathbb{D}$ regions in the limit $B \to B_c^-$. Denoting $1_{\mathbb{D}}(\xi)$ as the characteristic function that equals unity over the $\mathbb{D}$ regions and zero elsewhere, and noting that the $\mathbb{D}$ regions form when $\tau_S = -B$, we can write

$$F^* = F_{\mathbb{A}} + F_{\mathbb{D}} = \langle \tau_S(1 - 1_{\mathbb{D}}) \rangle + \langle \tau_B 1_{\mathbb{D}} \rangle = \langle \tau_B(1 - 1_{\mathbb{D}}) \rangle - B \langle 1_{\mathbb{D}} \rangle. \qquad (4.10)$$

Figure 15(*a*) includes a plot of F^* against B for the flux-less solutions ($B > B_c$) in the case with $D = 0$ and $\gamma = 4$. For $B > B_c$, F^* is negative, implying a consistent flux-less state. At $B = B_c$, F^* vanishes, corresponding to the breakup of the rigid regions and the generation of flux for $B < B_c$. Figure 16 displays computations of $B_c(\gamma, D)$, which we determined by locating the zero of F^* as B is varied over the flux-less solutions.

4.6. *Arrest of locomotion*

The arrest of locomotion at $B = B_s(\gamma)$ occurs when the remaining forwards-forced $\mathbb{A}$ region vanishes. In the limit $B \to B_s$, fluid motion takes place only in the vicinity of maximum forcing $\xi = \pi$, where the surface stress τ_S only slightly exceeds the yield stress, and $(Y_-, 1 - Y_+) \ll 1$. Guided by (2.22), we set

$$\tau_S = B + \mathcal{T}, \quad \tau_B \sim -B + \mathcal{T}, \quad p_\xi \sim 2B + \mathcal{T} \qquad (B \to B_s), \qquad (4.11a,b,c)$$
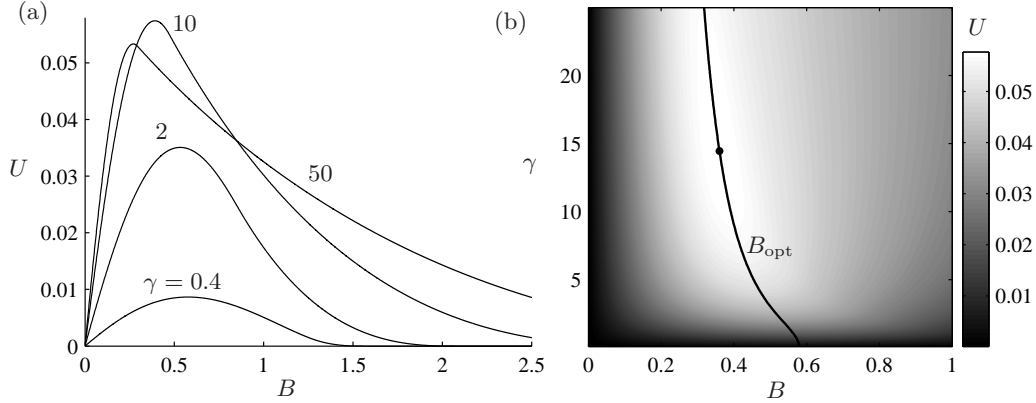
FIGURE 17. Locomotion speed U with $D = 0$ shown (a) as a function of Bingham number B for $\gamma = 0.4$, 2, 10 and 50, and (b) as a density over the (B, γ)-plane. In (b), the optimal Bingham number $B = B_{\mathrm{opt}}(\gamma, 0)$, which maximizes U for a given forcing parameter γ, is shown as a solid curve and the global maximum over all B and γ is indicated by a dot.
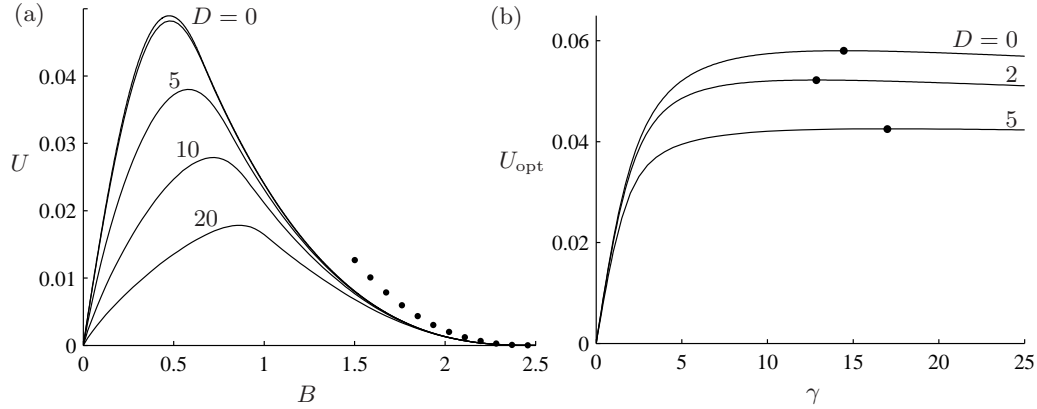

FIGURE 18. (a) Locomotion velocity U as a function of Bingham number B for $\gamma = 4$ and $D = 0$, 1, 5, 10 and 20. The asymptotic approximation for U close to the arrest of fluid motion (4.14) is shown as a dotted curve. Panel (b) shows the maximum speed over all Bingham numbers, $U_{\mathrm{opt}}(\gamma, D) \equiv \max_B U$, as a function of γ for stiffnesses of $D = 0$, 2 and 5. The dots show the global maxima.

where $\mathcal{T}(\xi) \ll B$. Substitution of (4.11a, b, c) into (A 1), we find that the leading-order surface velocity in the $\mathbb{A}$ regions simplifies to

$$u_S \sim -\mathcal{T}^2/4B \qquad (B \to B_s). \tag{4.12}$$

By substituting (4.12) into (4.6a), we deduce that $\Xi = O(\mathcal{T}^2)$, which, provided that D is order unity, implies that the elastic force in (2.24a) is negligible to leading order. Under this assumption, (2.24a) indicates that the muscular forcing directly prescribes the surface stress according to $\tau_S \sim f$. Combining this with (4.11a) and expanding f about $\xi = \pi$, we obtain

$$\mathcal{T} \sim f(\pi) - k(\xi - \pi)^2 - B \qquad (|\xi - \pi| < \zeta), \tag{4.13}$$

where $\zeta \equiv [(f(\pi) - B)/k]^{1/2}$ is the half width of the $\mathbb{A}$ region and $k \equiv f''(\pi)/2$.

Given that $\zeta = 0$ when $B = B_s$, we find that $B_s = f(\pi)$. Hence, fluid motion is arrested once the maximum of the forcing falls below the yield stress. The critical value $B_s(\gamma)$

is an increasing function of γ, reflecting the fact that forcing patterns with a stronger forwards-forced region generate locomotion more readily at larger yield stresses.

Finally, we determine the leading-order locomotion velocity as $B \to B_s$ by substituting (4.12) into (4.1b) to give

$$U = \langle u_S \rangle \sim \frac{1}{8\pi B_s} \int_{-\zeta}^{\zeta} (B_s - B)^2 \, \mathrm{d}\xi \sim \frac{(B_s - B)^{5/2}}{4\pi B_s k^{1/2}} \qquad (B \to B_s), \qquad (4.14)$$

which we plot as a dotted curve in figures 15(a) and 18(a).

4.7. *Optimization of locomotion*

In both the asymptotic limits $B \ll 1$ and $B \to B_s$, we found that locomotion is enhanced for larger values of γ. To determine whether this conclusion holds for intermediate values of B, we compute U as a function of B for various values of γ in the case $D = 0$. As shown in figure 17(a), increasing γ from zero initially has the effect of increasing U for all values of B. This trend continues until $\gamma \approx 14$, where $U_{\mathrm{opt}}(\gamma, 0) = \max_B(U) \approx 0.06$ is optimized over all γ at a Bingham number of $B = B_{\mathrm{opt}} \approx 0.34$. Although U_{opt} decreases with γ for $\gamma \gtrsim 14$, U still increases with γ for sufficiency small and large B, in accord with (4.8a) and (4.14). Thus, the advantage of increasing γ is limited for intermediate values of B. The maximization of U in the parameter space (B, γ) is illustrated further by the density plot of figure 17(b).

As indicated by figure 18(a), increasing the stiffness D decreases U for all values of B, suggesting that the perfectly flexible case is optimal for locomotion. This reflects the fact that the elastic force invariably resists tangential deformations of the surface of the foot. Nevertheless, the foot of a gastropod cannot be perfectly flexible and, as we showed in §4.2, the locomotor does not converge towards a steady state if $D = 0$. In order to optimize locomotion, gastropods may use the smallest D permissible subject to the material constraints of its anatomy.

Figures 17(a) and 18(a) illustrate that the maximum speed over all yield stresses U_{opt} depends on both the forcing parameter γ and the stiffness D. The plots of $U_{\mathrm{opt}}(\gamma, D)$ against γ for three different values of D in figure 18(b) demonstrate that this optimal speed becomes relatively insensitive to γ once that parameter is sufficiently large ($\gamma \gtrsim 10$). The global maxima of these curves, $U_{\mathrm{opt}}^*(D) = \max_{B,\gamma}(U)$, or maximum speed over all yield stresses and forcing parameters, are indicated by dots. With the typical values of γ close to these maxima, the forwards-forced regions of the forcing patterns span about one fifth of the spatial domain. This is comparable or slightly greater than the documented area of locomotive waves of terrestrial slugs and snails (Denny 1981; Lai *et al.* 2011). However, a substantial fraction of the foot of these gastropods is actually bordered by a rim that does not participate actively in locomotion.

In summary, our model predicts a maximum locomotion speed of $U \approx 0.06$ attained at the smallest possible stiffness D, a Bingham number of $B \approx 0.34$ and a forcing parameter of $\gamma \approx 14$. In terms of dimensional variables, this maximum speed translates to $0.06 \, \mathcal{A}_P H / \mu$, where $\mathcal{A}_P \equiv (T_+ - T_-)/f_P$ is the dimensional amplitude of the imposed forcing in (2.7). Notably, this maximum is independent of the wave speed c. Assuming that gastropods maximize their speed, and using the characteristic values of U, H and μ given in §2, we estimate that $\mathcal{A}_P \approx 2 \times 10^4$ Pa. This estimate is one order of magnitude larger than the direct stress measurements quoted by Denny (1981) and Lai *et al.* (2011). It seems unlikely, however, that such creatures are built for speed.

It is plausible that gastropods instead favour the optimization of mucus preservation. If this is the case, then the optimal parameter settings predicted by our model are simply those leading to a flux-less state with $B > B_c(\gamma, D)$, the outlines of which are illustrated

in figure 16. Even if $B < B_c$, the net flux is always small compared with the speed of locomotion, with the ratio Q/U having the maximum value $1/6$ in the Newtonian case, as indicated by figure 15 and $(4.8a, b)$. Therefore, the prograde strategy is essentially optimized for the preservation of mucus across the full range of parameter space.

5. Conclusions

Our goal in this article was to formulate a general model describing the mechanics of locomotion over a layer of viscoplastic fluid, and to compare the retrograde and prograde locomotion strategies employed by marine and terrestrial gastropods. Our solutions to the initial-value problem show that the locomotor undergoes an oscillatory convergence towards a steady state. In the retrograde case, the frequency of the oscillations equals that of the forcing wave, while in the prograde case it is inertio-elastic. In either case, the oscillatory transients are partly the result of a relatively sudden switch-on of the forcing in our computations. If the forcing waves are turned on more gradually, there are no transient oscillations, which is more in line with the gait of real biological organisms.

With the retrograde strategy, the yield stress always hinders locomotion, ultimately preventing it entirely beyond a critical Bingham number. That threshold corresponds to the formation of rigid plugs that span the depth of the mucus layer. The rigid plugs form underneath the most weakly forced sections of the foot. When this occurs, fluid is still yielded under the more strongly forced regions, resulting in peristaltic pumping of fluid in the direction of the waves.

With our prograde strategy, locomotion is impossible with Newtonian mucus. However, given a forcing pattern with forwards-forced regions that are narrower but stronger than the backwards-forced regions, the yield stress restricts more fluid motion in the backwards-forced regions, leading to a net forwards motion of the foot surface and hence locomotion. Beyond a critical yield stress, rigid plugs form across the mucus layer, blocking any flux of mucus in the direction opposite to that of locomotion; above a second threshold, the yield stress prevents backward motions of the foot altogether. By this stage, the yield stress impedes fluid flow only within the forwards-forced regions, and so locomotion speeds decline with any further increase of the yield stress. Locomotion is therefore maximized at an intermediate value of the Bingham number. Optimizing over all the parameters of the model, we find that the locomotion speed is greatest when the forwards-forced regions of the forcing pattern span about one fifth of a wavelength, and when the tangential stiffness of the foot is smallest.

Two key aspects of the locomotion of gastropods are the need to adhere to the substrate and to preserve mucus (Denny 1980). These requirements are all problematic for the retrograde locomotion strategy: there are no rigid plugs in the locomotive states to assist with adhesion and the retrograde waves pump a significant flux of mucus in the direction opposite to that of locomotion. In employing the retrograde strategy, it is possible that marine snails exploit the ambient Newtonian water to supplement mucus production. They also have a reduced need for adhesion because of buoyancy. By contrast, the requirements to adhere and preserve mucus are ideally suited to the prograde strategy employed by terrestrial gastropods. In this strategy, there is no conflict between adherence and locomotion, and the presence of rigid plugs also prevents any wasteful backwards flux of mucus.

Denny (1981) suggested that the primary reason for the slug *Ariolimax columbianus* to adopt the prograde strategy originated from the difficulty of the foot muscles in overcoming lubrication pressures in the mucus layer and lifting the foot vertically. However, Jones (1973) suggested that significant vertical displacements do occur during the loco-

motion of *Agriolimax reticulatus*, and the recent study of Lai *et al.* (2011) provides clear evidence for these in other gastropods. This issue could be further explored using the general model we formulated in §2, which allows for vertical displacements of the foot surface during prograde locomotion. Lai *et al.* (2011) also demonstrate that systematic variations occur within the envelope of the prograde wave train as one proceeds from the tail to the head of the gastropod, and detect fluid recirculations through the lateral rim of the foot, both of which could be modelled using the three-dimensional generalization of our model.

Finally, gastropod mucus undoubtedly has a more complicated rheology than that described by the Bingham model, including significant viscoelasticity and relaxation (Denny 1980; Ewoldt *et al.* 2007). Relaxation times of order one second are reported in the literature for snail mucus (see Ewoldt *et al.* 2007). The intrinsic time scale of our theoretical model $2\pi L/c$ is of order ten seconds given typical wave speeds of millimetres per second and wavelengths of order one centimetre. Hence, even though a time-dependent rheology may play a role, a first approximation based on the Bingham model seems justified.

Appendix A. Flow configurations

Denoting $\sigma \equiv \mathrm{sgn}(p_\xi)$, the velocity u, flux q and basal stress τ_B associated with the five possible flow configurations (2.23) are given by

$\mathbb{A}: 0 < Y_- < Y_+ < Y \quad (|\tau_B| > B, |\tau_S| > B, \tau_B\tau_S < 0),$

$$u = \begin{cases} u_P + \frac{1}{2}p_\xi(y - Y_+)^2, & Y_+ < y < Y, \\ u_P, & Y_- < y < Y_+, \\ u_P + \frac{1}{2}p_\xi(y - Y_-)^2, & 0 < y < Y_-, \end{cases} \quad u_P \equiv -\frac{1}{2}p_\xi Y_-^2, \qquad (\text{A 1})$$

$$q = \frac{1}{6}p_\xi[(Y - Y_+)^3 + Y_-^3 - 3Y_-^2 Y], \quad \tau_B = \frac{u_S p_\xi}{Y p_\xi - 2B\sigma} - \frac{1}{2}Y p_\xi. \qquad (\text{A 2})$$

$\mathbb{B}: Y_- < 0 < Y_+ < Y \quad (|\tau_B| < B, |\tau_S| > B),$

$$u = \begin{cases} \frac{1}{2}p_\xi(y - Y_+)^2, & Y_+ < y < Y, \\ 0, & 0 < y < Y_+, \end{cases} \qquad (\text{A 3})$$

$$q = \frac{1}{6}p_\xi(Y - Y_+)^3, \quad \tau_B = \sigma[B + (2u_S p_\xi)^{1/2}] - Y p_\xi. \qquad (\text{A 4})$$

$\mathbb{C}: Y_\pm < 0 \text{ or } Y < Y_\pm \quad (|\tau_B| > B, |\tau_S| > B, \tau_B\tau_S > 0),$

$$u = \frac{1}{2}p_\xi y(y - Y) + \frac{yu_S}{Y}, \quad q = \frac{1}{2}u_S Y - \frac{1}{12}p_\xi Y^3, \quad \tau_B = \frac{u_S}{Y} - \frac{1}{2}Y p_\xi + B\sigma. \qquad (\text{A 5})$$

$\mathbb{D}: 0 < Y_- < Y < Y_+ \quad (|\tau_B| > B, |\tau_S| < B),$

$$u = \begin{cases} u_S, & Y_- < y < Y, \\ u_S + \frac{1}{2}p_\xi(y - Y_-)^2, & 0 < y < Y_-, \end{cases} \qquad (\text{A 6})$$

$$q = -\frac{1}{6}p_\xi Y_-^2(3Y - Y_-), \quad \tau_B = -\sigma[B + (-2u_S p_\xi)^{1/2}]. \qquad (\text{A 7})$$

$\mathbb{E}: Y_- < 0 \text{ and } Y < Y_+ \quad (|\tau_B| < B, |\tau_S| < B), \; u = u_S = q = 0, \; \tau_B \text{ undetermined.}$

Appendix B. Low-amplitude retrograde locomotion

We develop an approximation for the steady locomotion velocity U in the simplified retrograde problem under the assumption that A and D are small. Neglecting the elastic force in (3.1b), we obtain the pressure gradient $p_\xi = -A\cos\xi$. Let

$$A \equiv \varepsilon^2, \quad B \equiv \varepsilon^3 B_3, \quad (U, Q) = \varepsilon^4(U_4, Q_4) + \cdots, \quad Y = 1 + \varepsilon^2 Y_2 + \varepsilon^3 Y_3 + \cdots, \quad \text{(B 1)}$$

where $\epsilon \ll 1$. In this small-amplitude limit, the flow is dominated by $\mathbb{A}$ regions, which are separated by two composite $\mathbb{D}$-$\mathbb{C}$-$\mathbb{B}$ regions surrounding the two locations $\xi = \pi/2$ and $3\pi/2$ where p_ξ changes sign. By combining (B 1) and (A 2), we can determine that

$$Y_2 = -\tfrac{1}{12}\cos\xi, \quad Y_3 = \tfrac{1}{4}B_3\sigma. \quad \text{(B 2)}$$

In the $\mathbb{A}$ regions, (A 2) provides the basal shear stress

$$\tau_B \sim \tfrac{1}{2}\varepsilon^2 Y\cos\xi + \varepsilon^4 U_4\left(\frac{|\cos\xi|}{|\cos\xi| - 2\varepsilon B_3}\right) \qquad (\mathbb{A}). \quad \text{(B 3)}$$

Noting that the edges of the $\mathbb{A}$ regions and the $\mathbb{D}$-$\mathbb{C}$-$\mathbb{B}$ regions occur where $|\tau_B| = B$ and $|\tau_S| = B$, we use (B 3) to determine that the latter occupy $|\xi - \pi/2| < \varepsilon\zeta$ and $|\xi - 3\pi/2| < \varepsilon\zeta$, respectively, where $\zeta \sim 2B_3 + 2(\varepsilon U_4 B_3)^{1/2}$. The $\mathbb{C}$ regions that lie between the $\mathbb{B}$ and $\mathbb{D}$ regions have widths of $O(\varepsilon^2)$ and hence are too narrow to contribute significantly to the force on the foot. Using (A 4) and (A 7), we can determine that the basal shear stresses in the $\mathbb{B}$ and $\mathbb{D}$ regions are given to leading order by

$$\tau_B \sim \begin{cases} \varepsilon^3 B_3 & (\mathbb{D}: \ \tfrac{1}{2}\pi - \varepsilon\zeta < \xi < \tfrac{1}{2}\pi), \\ \varepsilon^3 B_3 - \varepsilon^2(\xi - \tfrac{1}{2}\pi) & (\mathbb{B}: \ \tfrac{1}{2}\pi < \xi < \tfrac{1}{2}\pi + \varepsilon\zeta), \\ \varepsilon^3 B_3 + \varepsilon^2(\xi - \tfrac{3}{2}\pi) & (\mathbb{B}: \ \tfrac{3}{2}\pi - \varepsilon\zeta < \xi < \tfrac{3}{2}\pi), \\ \varepsilon^3 B_3 & (\mathbb{D}: \ \tfrac{3}{2}\pi < \xi < \tfrac{3}{2}\pi + \varepsilon\zeta). \end{cases} \quad \text{(B 4)}$$

Finally, substitution of (B 3) and (B 4) into the basal stress constraint (A 7) gives

$$U_4\left[1 - \frac{2}{\pi}\varepsilon B_3\log(\varepsilon^3 B_3 U_4)\right] \sim \frac{1}{48} - \frac{2}{\pi}B_3^2, \quad \text{(B 5)}$$

where the logarithmic term on the left-hand side originates from the integral of the last term on the right-hand side of (B 3). Recasting (B 5) in terms of the variables used in §3, we obtain (3.3). Note that the logarithmic dependence of U_4 on ε implied by (B 5) indicates that our construction cannot be viewed as a formal asymptotic expansion.

REFERENCES

BALMFORTH, N. J., COOMBS, D. & PACHMAN, S. 2010 Microelastohydrodynamics of swimming organisms near solid boundaries in complex fluids. *Quart. J. Mech. Appl. Math.* **63**, 267–294.

BALMFORTH, N. J. & CRASTER, R.V. 1999 A consistent thin-layer theory for Bingham fluids. *J. Non-Newt. Fluid Mech.* **84**, 65–81.

BIRD, R. B., DAI, G. C. & YARUSSO, B. J. 1983 The rheology and flow of viscoplastic materials. *Rev. Chem. Eng.* **1**, 1.

CHAN, D., BALMFORTH, N. J. & HOSOI, A. 2005 Building a better snail: lubrication theory and adhesive locomotion. *Phys. Fluids* **17**, 113101.

DENNY, M. W. 1980 The role of gastropod mucus in locomotion. *Nature* **285**, 160–161.

DENNY, M. W. 1981 A quantitative model for the adhesive locomotion of the terrestrial slug, *Ariolimax columbianus. J. Exper. Biol.* **91**, 195–217.

DENNY, M. W. & GOSLINE, J. M. 1980 The physical properties of the pedal mucus of the terretrial slug, *Ariolimax columbianus. J. Exper. Biol.* **88**, 375–393.

Ewoldt, R., Clasen, C., Hosoi, A. E. & McKinley, G. M. 2007 Rheological fingerprinting of gastropod pedal mucus and bioinspired complex fluids for adhesive locomotion. *Soft Matter* **3**, 634–643.

Hewitt, I. & Balmforth, N. J. 2012 Viscoplastic lubrication with application to bearings and mud washboards. *J. Non-Newtonian Fluid Mech.* **169170**, 74–90.

Holmes, S. P., Cherril, A. & Davis, M. S. 2002 The surface characteristics of pedal mucus: a potential aid to the settlement of marine orgainisms? *J. Mar. Biol. Ass. U.K.* **82**, 131–139.

Jones, H. D. 1973 Mechanism of locomotion of *Agriolimax reticulatus*. *J. Zool.* **171**, 489–498.

Katz, D. F. 1974 On the propulsion of micro-organisms near solid boundaries. *J. Fluid Mech.* **64**, 33–49.

Lai, J. H., del Alamo, J. C., Rodriguez-Rodriguez, J. & Lasheras, J.C. 2011 The mechanics of the adhesive locomotion of terrestrial gastropods. *J. Exper. Biol.* **213**, 3920–3933.

Prager, W. & Hodge, P. G. 1951 *Theory of perfectly plastic solids*. Wiley.

Shapiro, A. H., Jaffrin, M. Y. & Weinberg, S. L. 1969 Peristaltic pumping with long wavelengths at low Reynolds number. *J. Fluid Mech.* **37**, 799–825.

Takagi, D. 2009 Nonlinear peristaltic waves. *Proceedings of the Geophysical Fluid Dynamics Summer Study Program, Woods Hole Oceanopgraphic Institution* .

Taylor, G. I. 1951 Analysis of the swimming of microscopic organisms. *Proc. R. Soc. A* **209**, 447–461.

Tuck, E. O. 1968 A note on a swimming problem. *J. Fluid Mech.* **31**, 305–308.

Vajravelu, K., Sreenadh, S. & Babu, V. R. 2005 Peristaltic transport of a Herschel–Bulkley fluid in an inclined tube. *Int. J. Nonlinear Mech.* **40**, 83–90.